

# The highest-elevation frog provides insights into mechanisms and evolution of defenses against high ultraviolet radiation

**Ting-Ting Fu**

**Yan-Bo Sun**

State Key Laboratory of Genetic Resource and Evolution, Kunming Institute of Zoology, Chinese Academy of Sciences

**Wei Gao**

State Key Laboratory of Genetic Resource and Evolution, Kunming Institute of Zoology, Chinese Academy of Sciences

**Chengbo Long**

Kunming Institute of Zoology, Chinese Academy of Sciences

**Chun-Hua Yang**

State Key Laboratory of Genetic Resource and Evolution, Kunming Institute of Zoology, Chinese Academy of Sciences

**Xinwang Yang**

Faculty of Basic Medical Science, Kunming Medical University

**Yi Zhang**

State Key Laboratory of Genetic Resource and Evolution, Kunming Institute of Zoology, Chinese Academy of Sciences

**Xin-Qiang Lan**

Kunming College of Life Science, University of Chinese Academy of Sciences

**Song Huang**

College of Life Sciences, Anhui Normal University

**Jieqiong Jin**

Kunming Institute of Zoology, Chinese Academy of Sciences

**Robert Murphy**

Centre for Biodiversity and Conservation Biology, Royal Ontario Museum

**Yun Zhang**

Kunming Institute of Zoology, Chinese Academy of Sciences <https://orcid.org/0000-0002-8636-183X>

**Ren Lai**

Kunming Institute of Zoology

**David Hillis**

University of Texas at Austin <https://orcid.org/0000-0002-4787-0033>

**Ya-Ping Zhang**

Kunming Institute of Zoology <https://orcid.org/0000-0002-5401-1114>

**Jing Che** (✉ [chej@mail.kiz.ac.cn](mailto:chej@mail.kiz.ac.cn))

Kunming Institute of Zoology, Chinese Academy of Sciences

---

## Article

### Keywords:

**Posted Date:** March 28th, 2022

**DOI:** <https://doi.org/10.21203/rs.3.rs-1424490/v1>

**License:**  This work is licensed under a Creative Commons Attribution 4.0 International License. [Read Full License](#)

---

## Abstract

Defense against increasing ultraviolet radiation (UV) exposure is essential for survival, especially in high-elevation species. Although some specific genes involved in UV response have been reported, the full view of UV-defense mechanisms remains largely unexplored. Herein, we analyzed UV responses in the highest-elevation frog, *Nanorana parkeri*, using integrated approaches. We show less damage and more efficient antioxidant activity in skin of this frog than those of its lower-elevation relatives after UV exposure. Our study revealed new UV-defense systems. Genomic and metabolomic analysis along with large-scale transcriptomic and microRNA profiling revealed a time-dependent coordinated defense mechanism in *N. parkeri*. Both gene mutations and expression shifts contribute to such UV adaptation. We found that microRNAs play important regulatory roles, especially in decreasing the expression levels of cell-cycle genes. Moreover, multiple defense genes (i.e., *TYR* for melanogenesis) exhibit positive selection with function-enhancing substitutions. Our work demonstrates a genetic framework for evolution of UV-defense in a natural environment.

## Introduction

Ozone layer damage by human activities has significant effects on the environment, including an increase in the amount of UV radiation received at the surface of the Earth (1). Increased penetration of UV radiation is likely to have profound adverse impacts on human health as well as biodiversity (2). Exposure to intense UV can induce damage to DNA and oxidative stress through reactive oxygen species (ROS) in cells (3), which can lead to melanomas and other cutaneous diseases (4). Therefore, global increases in UV levels may pose a serious challenge to the health of organisms and maintenance of biodiversity. For these reasons, it is important to understand the genetic and molecular mechanisms used by organisms to cope with threats of increased UV.

Organisms have evolved a series of phenotypic and behavioral adaptations to counter the harmful effects of UV radiation. For example, bird feather colors, as well as human skin pigmentation, have evolved at least partly as adaptations to protect against UV radiation (5, 6). The adaptation of human skin pigmentation is related to the production and distribution of melanin, which can block or absorb light, and thereby prevent it from penetrating the skin (7, 8). There are differences in the degree of UV resistance among different species and populations, and high-elevation species typically have higher capability to block UV compared to low-elevation species (9, 10, 11), and such differences can be reflected at the molecular level (12). However, most recent molecular research on this problem has been restricted to UV exposure experiments on mouse or human cells in the lab. These studies have identified specific genes involved in antioxidant metabolism (8, 13, 14) and DNA repair (15, 16) pathways that can prevent or reduce UV-induced damage. Moreover, heat-shock proteins, such as hsp70, can bind to nucleic acid repair proteins after UV exposure in yeast, which is presumed to enhance DNA repair activity (17, 18). Nevertheless, we still lack a comprehensive understanding of UV defense mechanisms *in vivo*, including the diversity of defense pathways and genes and their dynamic evolution.

The Qinghai-Tibetan Plateau (QTP) is one of the areas with the most serious ozone layer depletion, which leads to high UV radiation intensity in this area (1). High-elevation species, such as the hot-springs snake and snub-nosed monkey, have evolved substitutions in their DNA-repair genes in response to long-term UV stress (12, 19). UV exposure is a particular challenge for amphibians compared to most other terrestrial vertebrates, as their skin is much thinner and lacks protective scales, fur, or feathers (20). Increased UV exposure can make amphibians more susceptible to pathogen infections (e.g., chytridiomycosis) and result in significant population declines (21, 22). Nevertheless, frogs of the genus *Nanorana* (Dicroglossidae) have colonized the QTP (at elevations up to 5,000 m) over the past 8–9 million years (23). One of the dominant species, *N. parkeri*, the world's highest-elevation frog, experiences much stronger UV radiation ( $\sim 3.5$  mW/cm<sup>2</sup> at  $\sim 4,500$  m) during daytime insolation than its lower-elevation relatives, such as *N. phrynoides* ( $\sim 1.6$  mW/cm<sup>2</sup> at  $\sim 1,700$  m) and *Quasipaa spinosa* ( $\sim 0.4$  mW/cm<sup>2</sup> at  $\sim 118$  m). Such long-term selective pressure acting on populations of *N. parkeri* resulted in a series of phenotypic adaptations in this species to potential UV defense, including increased skin pigmentation compared to its lower-elevation relatives (24). For these reasons, *N. parkeri* is an ideal model organism for studying the long-term adaptive strategies and the underlying genetic and molecular mechanisms related to UV-radiation protection.

In this study, we compare the Tibetan frog (*Nanorana parkeri*) with its lower-elevation relatives, using an integrated systems biology approach to study how various defense systems work together in organismal UV-defense. We dissect phenotypic changes and metabolomics, as well as the expression profile of genes and during UV exposure experiments. We then detect the positive selection signals across the genome. We further explore how the expression and sequences of these genes have evolved in response to adaptation to high UV radiation.

## Results

### Strong UV resistance is associated with efficient antioxidant activity in Tibetan frog skin

To clarify the details of the UV defense mechanism in *N. parkeri*, we separately exposed *N. parkeri* and its lower-elevation relatives to a time course of UV radiation at a dose of  $\sim 3.7$  mW/cm<sup>2</sup> (0, 0.5 h, 1 h, 2 h, 4 h, 6 h, and 8 h). Three to four individuals of each species were used per time point. The dose used was slightly higher than that of natural conditions of *N. parkeri* and the determination of maximal exposure time was based on maximal tolerances of individuals in pilot assessment (Methods). To observe morphological characteristics, a dorsal skin sample after UV exposure was taken from each individual for preparing a histological section. In total, at least 54 images were captured from each species to statistically quantify the skin structures and the degrees of damage to the skin morphology. Comparisons between the UV-exposed and unexposed skins further revealed that unexposed *N. parkeri* had a thin dermis with tightly connected cell layers; furthermore, the structures of the glands and the dense connective tissues

remained relatively compact and stratified in shape overall along with UV exposure (Fig. 1a; 1 h vs. 0 h:  $P = 0.12$ , > 1 h vs. 0 h:  $P < 0.05$  in Supplementary Fig. 1). In contrast, *Q. spinosa* (~118 m) possessed a less compact skin structure and the corresponding structures displayed considerable damage, including the destruction of glands, disruption of the calcified layer, and necrosis of the dermis, after UV exposure (Fig. 1a; 1 h vs. 0 h:  $P = 0.007$ , > 1 h vs. 0 h:  $P < 0.001$  in Supplementary Fig. 1). Similar skin morphology was also seen in another lower-elevation frog, *N. phrynoides* (~1,700 m) (Supplementary Fig. 1). These observations suggest that the skin of *N. parkeri* is more resistant to UV-induced necrosis compared to that of lower-elevation frogs.

We further examined the ROS-scavenging activity of skin secretions in *N. parkeri* and *Q. spinosa*, as antioxidant capacity was implicated in preventing oxidative damage from ROS after UV exposure (3, 14). The skin secretions were separately collected from individuals with UV exposure every 10 minutes and then repeated with an ABTS<sup>+</sup>-scavenging test. *N. parkeri* showed a significant increase in the ABTS<sup>+</sup>-scavenging activity after UV exposure and reached nearly 100% of the scavenging activity after ~30 minutes (Fig. 1b). In contrast, *Q. spinosa* exhibited a much smaller increase than *N. parkeri* after UV exposure and reached a maximum of only ~20% of the activity detected in *N. parkeri* (Fig. 1b).

Metabolomics analysis of skin samples (see Methods) provided more evidence for the comparatively efficient antioxidant activity in *N. parkeri*. After UV exposure, we identified intermediates of UV-screening melanin and antioxidant compounds (such as quinolinate and vitamins) (25, 26) in the skin secretions of *N. parkeri* that were absent in *Q. spinosa* (Fig. 1c, Supplementary Fig. 2 and Supplementary Data 2). The metabolism of *N. parkeri* and sustained high melanin content (Supplementary Fig. 3) were consistent with the UV-absorbing function of melanin (6). Moreover, after UV exposure, individuals of *N. parkeri* secreted more ( $\log_2(\text{FC}) > 1$ ,  $P < 0.05$ ) diverse neurotransmitters related to anti-inflammation and wound repair compared to unexposed frogs (Fig. 1c, Supplementary Fig. 2 and Supplementary Data 2). In contrast, we did not observe a similar change in *Q. spinosa* associated with UV exposure. These neurotransmitters included histamine (involved in wound repair and cell apoptosis) (27), ethoxyquin (an antioxidant) (28), and GABA (an anti-inflammatory compound) (29). The combined production of these compounds resulted in highly efficient antioxidant activity accompanied by immune modulation and anti-inflammatory effects, which together increase UV resistance in *N. parkeri*.

### Genome assembly of the Tibetan frog

We next explored the underlying genetic mechanisms of UV resistance in *N. parkeri*. To update the genome assembly of *N. parkeri*, we integrated the datasets generated by long-range PacBio RS II (21.3 million), short-read Illumina sequencing (328.62 Gb), chromatin conformation capture (Hi-C) (126 Gb), and genetic mapping (Supplementary Tables 1–5 and Supplementary Fig. 4). The genome size of the final assembly is approximately 2.46 Gb, which is close to the estimated size of 2.47 Gb from flow cytometry. The assembled genome has a high continuity with a contig N50 of 2.3 Mb and a scaffold N50 of 269 Mb, both of which are more than 250 times better than previous assembly (30) and exhibited the highest contig N50 among sequenced genomes of anurans (Supplementary Table 3). The contigs were anchored and oriented into 11 long pseudomolecules through a hierarchical clustering strategy (Supplementary Table 4). Furthermore, we identified 2,272 (87.9%, Supplementary Table 5) of the conserved vertebrate BUSCO genes, indicating the *N. parkeri* assembled genome is of high integrity and accuracy.

We annotated 22,884 nonredundant protein-coding genes based on an integration of methods, including *de novo*-based, homology-based, and transcriptome-based (Supplementary Tables 6 and 7). Furthermore, we annotated more than 1.3 Gb (55.2 % of the assembly) transposon elements and other non-coding RNAs throughout the genome assembly, including microRNA (miRNA), transfer RNA, ribosome RNA as well as small nucleolar RNA species (Supplementary Tables 8 and 9).

### Temporal expression patterns related to UV defense systems in Tibetan frog skin

All the individuals of *N. parkeri* and its lower-elevation relatives from the time-course UV exposure experiment (Fig. 2a) were separately submitted for RNA sequencing (RNA-seq) and transcriptomic analysis. We separately clustered the temporal expression profile of each species throughout the time-course using STEM clustering method (37). The STEM results suggest distinct patterns of gene expression in *N. parkeri*, including genes with continuous change during UV exposure (Profile #39 and #10 in Supplementary Fig. 6) and those upregulated at a specific time point (e.g., Profile #44, #43 and #27 in Supplementary Fig. 6). To precisely identify the co-expressed genes that are closely related to the time points of UV exposure, we further performed the temporal expression profile with WGCNA (32; Supplementary Fig. 7). After this sifting, we obtained four groups of genes in *N. parkeri* that are characterized by time sequence in expression, including groups of early-phase (0.5 h) up-regulation, later-phase (6–8 h) up-regulation, gradual increase throughout the UV exposure period, and gradual decrease throughout the UV exposure period. We then conducted Gene Ontology (GO) functional enrichment analyses for the co-expressed genes in each temporal group.

In the early-phase up-regulation group, genes associated with the immune system and skin moisturizing, such as *F2RL1*, *IL12B*, *DEGS2* and *PGLYRP3* (33, 34, 35; Supplementary Data 4) were upregulated in *N. parkeri*, followed by a moderate decrease in expression to their initial expression levels (Fig. 2b and Fig. 3a). These immune genes are involved in complex cascades including cytokine production, IL-1/6/8/17 secretion, T cell and mast cell activation, the NOD-like signaling pathway, and the NF- $\kappa$ B signaling pathway (Supplementary Data 4). These results suggest that the initial activation of immunity protects *N. parkeri* from UV-induced immunosuppression, which would otherwise be a source of damage during early UV exposure (21). Genes related to the regulation of moisturization also showed increased expression during this period (Supplementary Data 4). These included genes involved in the biosynthesis of ceramide, which functions in constructing moisturizing screen through working with saturated fatty acids and promotes profound cell pro-apoptosis through regulating relative pathways in response to UV-induced oxidative stress (36). In contrast, most orthologous genes in *Q. spinosa* (~118 m) did not exhibit obvious changes in expression (Fig. 2b). We also performed the same experimental procedures and analyses on

lower-elevation *N. phrynooides* (~1,700 m), and found that some orthologs of genes that are up-regulated in *N. parkeri* early in UV exposure actually exhibit decreasing expression in *N. phrynooides* (Supplementary Fig. 8 and Supplementary Data 4).

For the later-phase up-regulation group, co-expressed genes that are involved in inflammation and apoptosis regulation displayed significant up-regulation in *N. parkeri*, especially among genes related to histamine secretion, autophagy, and leukocyte activation (Fig. 2b, Fig. 3b and Supplementary Data 5). The up-regulation of these pathways is closely related to the early cellular changes during the exposure, such as the accumulation of damaged cells and the expression of chemokines that were secreted by immune cells. Increases in the expression of related genes, including *SNAP23*, *SLC22A3*, and *SNX6* (37, 38, 39), potentially explained the observed higher abundance of histamine in the metabolome of *N. parkeri* compared to *Q. spinosa* after long UV exposure (Fig. 1c). The other subgroup of co-expressed genes related to antioxidant metabolism, including genes involved in the production of melanin and nicotinamide salvaging, also showed increased expression after prolonged UV exposure in *N. parkeri* (Fig. 3b and Supplementary Data 5). This is reminiscent of the observed retention of high pigment content (Supplementary Fig. 3) and increased antioxidant production in the metabolome of *N. parkeri* after long UV exposure. However, these late-phase up-regulated orthologs displayed up-regulation just in early phase of UV exposure in *Q. spinosa* (Fig. 2b) or a slight decrease in *N. phrynooides* (Supplementary Fig. 8 and Supplementary Data 5).

Genes responsible for heat stress response (such as those encoding heat-shock proteins HSP90AA1 and HSF3) exhibited gradually increased expression in *N. parkeri* skin with ongoing exposure to UV, whereas the orthologous genes of the lower-elevation relatives exhibited no obvious change in expression (Fig. 2b, Fig. 3c and Supplementary Fig. 8). It is reasonable that UV-exposure associated with heat production imposes major stress, especially in poikilotherms such as frogs. Given that heat-response genes function to relieve stress and regulate ATPase to protect proteins from unfolding (17, 18), they are important for determining the critical thermal maximum of organisms. The other set of gradually up-regulated genes found in *N. parkeri*, such as *ADCYAP1*, *SSTR2* and *CHRNA6*, are relevant to regulation of the peripheral nervous system (the neuropeptide signaling pathway and neurotransmitter biosynthesis) (40, 41, 42, Supplementary Data 6). This finding is in accord with the abundant number of neurotransmitter metabolites identified in *N. parkeri* (Fig. 1c and Supplementary Data 2). Neurotransmitters transmit chemical signals across synapses between neurons and other types of cells, and neuropeptides are involved in mediating UV-induced suppression of immune cells responses (43). These genes may also sustain an efficient mechanism whereby *N. parkeri* rapidly transfers antioxidants as well as other metabolites between types of cells. However, the orthologs of these genes were only up-regulated in late phase of UV exposure in *Q. spinosa* (Fig. 2b) or decreased in expression in *N. phrynooides* (Supplementary Fig. 8).

Conversely, the co-expressed genes in the gradually decreased expression group of *N. parkeri* are involved mostly in cell cycle regulation (Fig. 2b and Fig. 3d). The orthologs of these genes in the lower-elevation relatives showed little change in their patterns of expression (Fig. 2b and Supplementary Data 7). These genes may be down-regulated during UV exposure in *N. parkeri* to prevent the cells from erroneously moving through the cell cycle during apoptosis (44). The repression of the expression of genes involved in the cell cycle occurs in parallel with apoptosis, which has been associated with local adaptation to UV radiation in diverse human populations (45).

### miRNAs serve as regulatory modulators of gene expressions in UV defense systems

To further explore the noncoding regulatory modulators that might induce the observed temporal expression, we performed miRNA-seq for the same individuals of *N. parkeri* and its lower-elevation relatives from the UV exposure time-course experiment. miRNAs are commonly implicated in the regulation of stress responses mainly by silencing mRNA expression. Combining predictions from the *N. parkeri* genome and miRNA-seq data, we respectively identified 515 miRNAs in *N. parkeri*, 76 in *Q. spinosa* (~118 m), and 116 in *N. phrynooides* (~1,700 m) (Supplementary Fig. 9 and Supplementary Data 8). Then the target genes were predicted and the miRNA candidates that were co-expressed with target genes in each of the four temporal groups were identified. Some unique miRNAs found only in *N. parkeri* (Fig. 4a and Supplementary Data 8), such as miR-3617-3p and miR-4440, were associated with target genes belonging to the later-phase up-regulation group (MM = -0.67 and  $P = 0.0016$  for miR-3617-3p; MM = -0.6 and  $P = 0.006$  for miR-4440 in Supplementary Fig. 10). These miRNAs did not show conspicuous changes in expression until 8 h after UV exposure and were followed by a decrease, which was the opposite pattern of the up-regulation of inflammation and immune regulation genes in the same phase. Other *N. parkeri* unique co-expressed miRNAs, such as miR-1288-3p and miR-6587-5p, are predicted to drive the reduced expression of cell cycle genes (Fig. 4b, Supplementary Fig. 11 and Supplementary Table 11). The expression of these miRNAs gradually increased and showed a significant negative correlation with that of their predicted target genes (*NFIL3*, *RNF212*, *CLEC10A* and *CRP* for miR-1288-3p and *CDT1* and *LRRFIP2* for miR-6587-5p) (Fig. 4b and Supplementary Table 11).

Some miRNAs that can be found in *N. parkeri* and its lower-elevation relatives showed distinctly different expression patterns in *N. parkeri*. For instance, miR-4762-3p and miR-5186 are co-expressed miRNAs associated with genes in the gradually decreasing expression group of *N. parkeri*, whereas miR-4762-3p only expressed around 1 h and 2 h of UV exposure in *N. phrynooides* and *Q. spinosa*, respectively. miR-5186 showed no clear expression patterns in both lower-elevation relatives (Supplementary Fig. 12). Our results indicated that miRNAs contribute to the temporal expression of UV defense genes, especially for cell-cycle-related genes in *N. parkeri*.

### UV pressure has driven the positive selection of defense genes in *N. parkeri*

After discovering the temporal expression changes between species in UV defense genes, we examined differences in genes and proteins sequences themselves to determine how they might affect functional changes. Genes with an increase in the ratio of nonsynonymous: synonymous substitutions

are often associated with selection pressure (such as from UV stress). Based on the phylogenetic relationships among the studied frogs (46), we applied the improved branch-site likelihood-based test (47) on their orthologs to detect positively-selected genes (PSGs) in *N. parkeri*. We identified a total of 554 PSGs in *N. parkeri* (Supplementary Data 10). These PSGs were significantly enriched in functional terms related to the UV defense systems identified above, including the immune response, ceramide catabolism, antioxidant metabolism (involved in pigment biosynthesis, vitamins, and nicotinamide metabolism), heat-shock response, and DNA damage response (Table 1 and Supplementary Data 10). Some of these PSGs also belong to the specific temporal expression groups described above (Table 1), further confirming that they are not only closely related to response to UV exposure in expression, but also play an important role in UV adaptation through sequence evolution.

*TYR*, as an example of PSGs, encodes a rate-limiting tyrosinase involved in melanin biosynthesis (48). The protein encoded by this gene (*TYR*) acquired three significant amino-acid replacements (N333S, F364L and S384G) along the *N. parkeri* lineage (Fig. 5a and Supplementary Fig. 13). Among the three replacements, S384G resulted in a change in the polarity of the encoded amino acid that is located at a functional domain of *TYR*, located outside the cell membrane. We thus hypothesized that the modified *TYR* in *N. parkeri* may have higher affinity with its substrate L-DOPA. To test this hypothesis, we separately synthesized the protein sequence of *TYR* of both *N. parkeri* and *Q. spinosa* *in vitro*, then performed enzyme kinetic analyses for these proteins with the substrate L-DOPA and measured at 1-minute intervals. These analyses revealed a lower *K<sub>m</sub>* (Michaelis constant) value ( $0.130 \pm 0.073 \text{ mM}\cdot\text{L}^{-1}$ ) of the amino-acid-replacement-bearing tyrosinase in *N. parkeri* compared to that in *Q. spinosa* ( $0.1663 \pm 0.117 \text{ mM}\cdot\text{L}^{-1}$ ) (Fig. 5b), indicating that the identified replacements confer a higher enzymatic affinity on the *TYR* protein. In parallel, the increase in *TYR* expression was sustained over the course of UV exposure, in coordination with the up-regulated expression of other genes (e.g., *SLC45A2*) that transport substances required for melanin production. This suggests that the *TYR* gene of *N. parkeri*, with its function-enhancing substitutions, plays an important role in adaptation of constitutive darker coloration and persistent melanin production in this species during UV exposure. Hence, both gene sequence variations and temporal expression shifts contribute to adaptation and better resistance to UV exposure in *N. parkeri*. Beside *TYR*, other PSGs in *N. parkeri* also showed distinct sequence substitutions from other four lower-elevation relatives (*N. medogensis*, ~2,900 m; *N. phrynoides*, ~1,700 m; *Q. spinosa*, ~118 m), including *MARS*, *CYB5R3* and *MGST3*. This result suggests these PSGs that evolved with rapid rates may play an important role in long-term adaptation of *N. parkeri* to high elevation (Supplementary Fig. 14).

## Discussion

Many species, including humans, are facing increased surface UV exposure as a result of anthropogenic environmental change. There has been accumulating evidence showing that the growing UV exposure contributes to global biodiversity loss, as well as human skin cancers (49). Thus, it is crucial to understand the genetic basis underlying organismal adaptations to UV exposure. Most investigations have used skin cells of model species that are not well-adjusted to UV radiation to explore genetic responses. This has intrinsically set limitations to our understanding of how genetic modulations in an organism could effectively protect itself from UV-induced damages.

*Nanorana parkeri*, an endemic frog of the high-elevation Qinghai-Tibetan Plateau (23), has evolved adaptations to perennial strong UV radiation at high elevations and hence provides an excellent model system for studying UV defense. UV adaptations of *N. parkeri* include various types of phenotypic changes, especially increased melanin accumulation in skin (Supplementary Fig. 3) and efficient UV resistance (Fig. 1), as demonstrated in this study. Genomic and transcriptomic analyses further showed that its UV adaptation results from accumulation of gene sequence changes (i.e., positive selection on the UV-defense genes), as well as by gene regulation changes in defense networks, especially when the host is facing long UV exposure.

We identified new systems in *N. parkeri* that have not been previously reported as involved in UV defense, such as peripheral nervous systems and heat-stress responses (Fig. 3 and Fig. 6). The immunomodulation and anti-inflammation roles of diverse neurotransmitters (such as histamine) in UV response has been little explored in previous studies. During UV defense, the immune system and moisturization were activated in the early phase of UV exposure to form a protective screen for skin, followed by the response of the antioxidation system (Fig. 6). The anti-inflammation system was also induced during UV exposure, likely by chemokines secreted by the activated immune cells in early phases of exposure (Fig. 6). Genes associated with the heat-stress response and the peripheral nervous system gradually increased in expression to separately deal with increasing heat production and the transfer of immune and anti-inflammation related neurotransmitters; meanwhile, cell-cycle associated genes gradually decreased in expression, in a manner consistent with apoptosis (Fig. 6). In contrast to the considerable observed changes in gene regulation during UV exposure in *N. parkeri*, we observed much less temporal expression regulation in orthologs of lower-elevation relatives, e.g., *N. phrynoides* (~1,700 m) and *Q. spinosa* (~118 m) (Fig. 2b, Supplementary Data 4). Some of the genes we identified as involved in UV defense in *N. parkeri* have been reported as involved in UV adaptation of other high-elevation species, such as *CCNT2* and *DMAP1* in the Tibetan hot-spring snake (19), as well as *CDT1* and *RTEL1* in snub-nosed monkeys (12). Our results further showed the dynamic regulation of these genes in *N. parkeri* in response to UV exposure. For example, *CCNT2* and *DMAP1* are up-regulated for DNA repair in *N. parkeri*, whereas *CDT1* and *RTEL1* contributed to DNA replication regulation and are among the down-regulated genes (Supplementary Fig. 15). In contrast, in *N. phrynoides*, *CCNT2*, *CDT1* and *RTEL1* fluctuated toward a decreasing trend and *DMAP1* shifted dramatically in expression during UV exposure (Supplementary Fig. 15). In *Q. spinosa*, all these genes showed a reduction trend of expression (Supplementary Fig. 15 and Supplementary Data 4).

Previous studies based on mammalian and yeast cells have separately identified single genes or exogenous chemical compounds that are involved in mitigating UV-induced damage, including those related to melanogenesis (50, 51, 52), vitamin synthesis (53, 54) and DNA repair (55, 56). However, UV defense is not determined by a single gene but by a suite of genetic adaptations acting in concert. Here, we used *N. parkeri* to systematically demonstrate how various defense genes, including PSGs and temporal expression genes, have evolved to work together in an organism to protect its

skin from UV damage. Although some functions of these individual defense genes have been identified by previous studies, we demonstrate that UV defense involves the cooperation among many different systems and genes. For example, the gene *TYR* has been reported to play a key role in melanogenesis and skin disease (46). In this study, we observed that *TYR* as well as other genes in melanogenesis (*GNAS*, *EP300*, *GSK3B*, *PLCB*) are PSGs and evolved rapidly in *N. parkeri* (Supplementary Data 10). *TYR* is up-regulated gradually during UV exposure and works with up-regulated *SLC45A2* to induce melanosomes to produce p-hydroxyphenylacetothiohydroximate, which is necessary for melanin generation. The up-regulation of both genes is associated with upregulation of genes upstream, including *CREBL2* and *EP300* (Supplementary Fig. 16). This process may also trigger observed up-regulation of the TC-NER master organizing protein gene *ERCC6* (involved in DNA repair; 57) and *CRTC3* (involved in cell cycle regulation and melanogenesis; 58) (Supplementary Fig. 16). However, in *N. phrynoides*, *TYR* is only up-regulated at ~ 4 h of UV exposure and *EP300* was only upregulated at 8 h, while *CREBL2* fluctuated in expression. In *Q. spinosa*, *TYR* was up-regulated for the first 1 h and then gradually downregulated, and other genes including *SLC45A2*, *CREBL2* and *EP300*, showed a trend of decrease in expression (Supplementary Fig. 16 and Supplementary Data 4).

Our results revealed that in addition to substitutions in genes of *N. parkeri*, temporal expression changes of some genes are regulated by miRNAs, especially in cell cycle genes. In cell cycle signaling of *N. parkeri*, PSGs such as *CREBBP* and *EP300* induce cell apoptosis. *BUB1* and another PSG *SMC1A* regulate the cohesion formation, which is critical for DNA duplication. PSG *GSK3B* works with downstream genes with a gradual decrease in expression, which directly affects DNA biosynthesis. MiRNAs were involved in regulating expression of these downstream genes, including miR-744-3p for *BUB1* and *E2F3*, miR-5186 for *ORC6* and *MCM4*, miR-4762-3p for *DBF4*. All these miRNAs showed gradual increase in expression and inhibited their target genes during UV exposure. However, miR-744-3p has not been identified in lower-elevation relatives. In *N. phrynoides*, miR-5186 fluctuated toward a trend of decrease in expression and miR-4762-3p was not expressed except with a slight up-regulation at 1 h of UV exposure. The target genes (*ORC6* and *MCM4*) also fluctuated in expression (Supplementary Fig. 12). In *Q. spinosa*, miR-5186 dropped in expression until 2 h of UV exposure and then was slightly upregulated, and miR-4762-3p showed little expression. Their target genes either did not present any compensatory change or exhibited a tendency to decrease in expression (Supplementary Fig. 12).

The UV-adaptations of high-elevation *N. parkeri* provide compelling insights into how some species may adapt to environmental changes in UV exposure. The mechanisms and pathways that we have identified may also be useful to understand the regulatory mechanisms underlying skin physiology and complex diseases, such as melanoma. This study contributes to our understanding of UV defense and provides a model for the study of defense against other environmental stresses.

## Methods

### Sampling information and ethics statement

Collection localities and treatments for all samples are given in **Supplementary Table 1**. The collecting permit and all study protocols were approved by the Animal Care and Ethics Committee of Kunming Institute of Zoology, Chinese Academy of Sciences, and were conducted in strict accordance with the guidelines for Animal Care and Use at the Kunming Institute of Zoology (SMKX-20160301-03).

To exclude potential influences of sex differences and developmental stages, we only collected male adults during their reproductive periods for all the studied frogs. Captured frogs were housed in artificial ponds with sufficient food at appropriate temperature. At least three individuals with identical treatment were sampled, and the mean snout-vent lengths of each species (*N. parkeri*: 4.300 ± 0.2 cm; *N. phrynoides*: 8.2 ± 0.4 cm; *Q. spinosa*: 8.7 ± 0.2 cm; mean ± SD) were measured using a digital Vernier caliper to ensure they were of similar age. After the frogs were sacrificed, their dorsal skin was isolated rapidly for subsequent analyses.

### UV exposure experiments and skin samples collection

To set the UV dosage used in the experiments, we obtained illumination photometry measurements of local habitats of the studied species using an illuminometer (TES-1339, TAIWAN) and then referred to previous research (11) based on the proportion between elevation and illumination. We used a dose of ~3.7mW/cm<sup>2</sup> UV exposure in experiments, which is slightly higher than the daily illuminance of local conditions that *N. parkeri* experiences (~3.5mW/cm<sup>2</sup>). In the pilot assessment of tolerance to UV, we exposed individuals of studied frogs to a continuous ~3.7mW/cm<sup>2</sup> UV light until a demise was observed. At the 8 h of UV exposure, we observed the first demise in *N. phrynoides* and serious skin peeling in *Q. spinosa*, whereas individuals of *N. parkeri* showed no behavioral signs of distress and exhibited only mild skin peeling. Hence, continuous UV exposure (up to 8 h) at a dose of ~3.7mW/cm<sup>2</sup> was established for use in the time-course UV exposure experiments.

In the UV-exposure experiment, three to four male adults of *N. parkeri* and its lower-elevation relatives were washed by ddH<sub>2</sub>O and set in a plastic box (20 x 15 x 15 cm) filled with 200ml ddH<sub>2</sub>O. Then we exposed individuals (n = 27 for *N. parkeri* and *N. phrynoides*, n = 20 for *Q. spinosa*) to UV light at a dose of ~3.7mW/cm<sup>2</sup> following a time course (0, 0.5, 1, 2, 4, 6 and 8 h). Frogs in the same box were treated with identical exposure time (at a time point). 50 μL ddH<sub>2</sub>O samples containing skin secretions were collected separately from the groups from 0 h to 8 h at intervals of 10 minutes to evaluate their ABTS<sup>+</sup> free radical-scavenging activities. Dorsal skin samples of individuals were collected separately from same position for the subsequent identification of metabolic compounds, histological analysis, and mRNA and miRNA sequencing.

### Statistical analysis of changes to skin histology

To examine skin structure, we collected dorsal skin samples near the foramen magnum in a 1 cm x 1 cm square immediately after the frogs were sacrificed and subjected them to hematoxylin-eosin (HE) staining procedures (17). The skin tissues were fixed in 10% buffered formalin overnight and subsequently preserved in 70% ethanol for storage under ambient conditions. The tissues were then embedded in paraffin. Histological sections with 6  $\mu\text{m}$  thickness were removed on positively charged slides, which were then stained with the HE solution. All the tissue samples were examined and photographed in a blinded manner. Images of each histological section were captured by a Leica DM4000B microscope (Leica, Heidelberg, Germany) at  $\times 100$  or  $\times 200$  magnification. All the skin morphological characteristics, including melanin content and the proportion of necrotic areas, were quantified based on images of HE stained sections with Pro-Plus® (IPP) version 6.0 (<http://www.mediacy.com/imageproplus>). All the images used to statistics are given in **Supplementary Data1**.

After capturing images of histological sections at  $\times 200$  magnification, at least 3 images of each individual were stochastically selected to quantify damage degree and melanin content. Hence, a minimum of 54 images from each species (from 6 time points of UV exposure experiment) were used for statistical analysis. For each histological image, the proportion of hollowed-out areas within the overall epithelial area was calculated to measure the degree of damage (%). For melanin content assessment, chromocytes were identified by comparing the integrated optical density and the background. The mean integrated optical density (MIOD) (59) for each image was measured to represent melanin content in skin. After quantification of skin structures, a two-tailed *t*-test was used for significance testing.

### Measurement of ABTS<sup>+</sup> free radical-scavenging activities

The collected solutions containing skin secretions were centrifuged at 12,000rpm, 4°C for 10 minutes, and then the supernatants were lyophilized and stored at -80°C until use. A 2, 2'-azino-bis (3-ethylbenzothiazoline-6-sulfonic acid) (ABTS) scavenging test (60) with some modification was adopted to evaluate the antioxidant activity of the samples. Briefly, a stock solution of ABTS radical (Sigma-Aldrich, USA) was prepared by incubating 2.8 mM potassium persulfate (Sigma-Aldrich, USA) with 7 mM ABTS in water for at least 6 hours in the dark, after which it was used immediately. The stock solution was diluted 50-fold with ddH<sub>2</sub>O, and then 50  $\mu\text{L}$  samples were added to the diluted stock solutions and kept from light for 30 minutes, with a blank control of same volume of ddH<sub>2</sub>O. Vitamin C (Sigma-Aldrich, USA) dissolved in H<sub>2</sub>O was used as the positive control. The decrease in absorbance at 415 nm indicated the antioxidant activity of the samples. The rate of free radical scavenging (%) was calculated as follows:  $(A_{\text{blank}} - A_{\text{sample}}) \times 100 / A_{\text{blank}}$ .

### Metabolite identification and quantification

Each skin sample (100 mg) was ground with liquid nitrogen and homogenate was resuspended with prechilled 80% methanol and 0.1% formic acid by well vortex. The samples were incubated on ice for 5 min and then were centrifuged at 15,000 g, 4°C for 20 min. Some of supernatant was diluted to final concentration containing 53% methanol by LC-MS grade water. Then supernatant was subsequently transferred to a fresh Eppendorf tube and centrifuged at 15000 g, 4°C for 20 min. Finally, the supernatant was injected into the LC-MS/MS system analysis (61).

UHPLC-MS/MS analyses were performed using a Vanquish UHPLC system (ThermoFisher, Germany) coupled with an Orbitrap Q Exactive<sup>TM</sup>HF-X mass spectrometer (Thermo Fisher, Germany) in Novogene Co., Ltd. (Beijing, China). Samples were injected onto a Hypesil Gold column (100 $\times$ 2.1 mm, 1.9 $\mu\text{m}$ ) using a 17-min linear gradient at a flow rate of 0.2mL/min. The eluents for the positive polarity mode were eluent A (0.1% FA in water) and eluent B (methanol). The eluents for the negative polarity mode were eluent A (5 mM ammonium acetate, pH 9.0) and eluent B (methanol). The solvent gradient was set as follows: 2% B, 1.5 min; 2-100% B, 12.0 min; 100% B, 14.0 min; 100-2% B, 14.1 min; 2% B, 17 min. Q Exactive<sup>TM</sup>HF-X mass spectrometer was operated in positive/negative polarity mode with spray voltage of 3.2 kV, capillary temperature of 320 °C, sheath gas flow rate of 40 arb and aux gas flow rate of 10 arb.

The raw data files generated by UHPLC-MS/MS were processed using Compound Discoverer 3.1 (CD3.1, ThermoFisher) to perform peak alignment, peak picking, and quantitation for each metabolite. The main parameters were set as follows: retention time tolerance, 0.2 minutes; actual mass tolerance, 5ppm; signal intensity tolerance, 30%; signal/noise ratio, 3; and minimum intensity, 100,000. After that, peak intensities were normalized to the total spectral intensity. The normalized data was used to predict the molecular formula based on additive ions, molecular ion peaks and fragment ions. And then the peaks were matched against the mzCloud (<https://www.mzcloud.org/>), mzVault and Mass List database to obtain the accurate qualitative and relative quantitative results. Statistical analyses were performed using the statistical software R (version R-3.4.3), Python (v 2.7.6) and CentOS (CentOS release 6.6).

The metabolites were annotated using the KEGG (Kyoto Encyclopedia of Genes and Genomes) database (<https://www.genome.jp/kegg/pathway.html>), HMDB database (<https://hmdb.ca/> metabolites) and LIPIDMaps database (<http://www.lipidmaps.org/>). Principal components analysis (PCA) and Partial least squares discriminant analysis (PLS-DA) were performed at metaX (a flexible and comprehensive software for processing metabolomics data). We applied univariate analysis (two tailed *t*-test) to calculate the statistical significance (*P*-value). The metabolites with *P*-value < 0.05 and fold change (FC)  $\geq 2$  or  $\leq 0.5$  were considered to be differentially expressed metabolites (DEMs). The functions of these metabolites and metabolic pathways were studied using the KEGG database (**Supplementary Fig. 2**).

### Genome sequencing, assembly and annotation

One female *N. parkeri* from Lhasa, Tibet Autonomous Region (~3,697m) of China was prepared for DNA isolation (**Supplementary Table 1**). After euthanasia, liver, muscle, heart, lung, brain, skin, kidney, and ovary tissues were deprived and stored in liquid nitrogen. Briefly, genomic DNA for SMRT bell library construction was extracted from liver with QIAGEN® Genomic DNA extraction kit. Total RNA was extracted from each of the above tissues using TRIzol reagent (Invitrogen Corp., Carlsbad, CA) and RNeasy Mini Kit (Qiagen, Chatsworth, CA).

For long-read sequencing, SMRTbell libraries with fragment size of 20 kb were constructed with SMRTBell template preparation kit 1.0 (Pacific Biosciences, Menlo Park, CA, USA). The libraries were sequenced by the PacBio Sequel system (Pacific Biosciences) with 25 SMRT cells. This generated 237.27 Gb of PacBio long-read data (21.25 million reads) with N50 > 17 Kb. These data were *de novo* assembled to obtain a preliminary *N. parkeri* genome (approximately 2.46Gb) with Falcon (62) and contig N50 was 2.32 Mb. To estimate genome size and perform error correction of the assembled genome, short-read sequencing data were obtained based on a paired-end library with short insert sizes of about 350 bp. Raw reads were produced using BGISEQ-500 platform, with read lengths of 2×150 bp. SOAPnuke (63) software was used to filter adapter and low-quality data.

To obtain a chromosome-level assembly, the Hi-C technique was applied to capture genome-wide chromatin interactions. Genomic DNA in muscle samples was fixed with formaldehyde in a concentration of 1% to allow cross-linking of cellular protein. Three Hi-C libraries were prepared following the standard Hi-C library protocol. Then we used BGISEQ-500 platform to sequence the libraries with paired-end 100 bp reads. Same to short-read sequencing, SOAPnuke was used to filter adapter and low-quality data, and then the Hi-C reads were evaluated and further filtered by HiC-Pro (64). Approximately 394.87 Gb clean data were generated.

For transcriptome sequencing, a single pooled RNA sample was prepared by mixing equal volumes of the RNA extracted from each tissue. Total RNA was synthesized to the first-strand cDNA using Clontech SMARTer PCR cDNA Synthesis Kit. After PCR Optimization, a large-Scale PCR was performed to synthesize second-strand cDNA. After another large-Scale PCR, the DNA was used for SMRTbell library construction. Qualified sequencing data were obtained by sequencing this library using PacBio Sequel platform. To obtain consensus full-length isoforms, we performed SMRT analysis through Reads of insert, Classify, Cluster, and Quvier.

To estimate the genome size and heterozygosity of the *N. parkeri* genome, a k-mer depth frequency distribution analysis (with k=17) of the short-read sequencing data was performed. After polishing the primary assembly using both PacBio long-read data and BGISEQ short-read data with Pilon (65), we got a high quality contig level genome of *N. parkeri*. The finally total length of the *N. parkeri* genome was 2.47 Gb, with a contig N50 of 2.34 Mb (**Supplementary Table 2**). We used BUSCO (66) to evaluate the finally obtained contig-level assembly. This analysis showed that 93.5% of the orthologous genes were retrieved in the assembly, including 87.9% complete genes and 5.6% fragmented genes (**Supplementary Table 3**). To perform chromosome-level assembly of the genome based on chromatin conformation capture technology, Lachesis (67) was used to cluster, order, and orient the contigs based on valid reads of Hi-C. Finally, we obtained 13 pseudochromosomes with a genome size of 2.47 Gb and scaffold N50 of 268.57 Mb, which is the first chromosome-level high-elevation amphibian genome (**Supplementary Tables 4 and 5, Supplementary Fig. 4**).

*De novo*-based, homology-based, and RNA sequence-based methods were used to annotate the positions and structures of protein-coding genes. *De novo* prediction was performed using Augustus (68). For homology-based prediction, homologous gene sets of the protein gene sets from *Homo sapiens*, *Gorilla gorilla*, *Macaca mulatta*, *Mus musculus*, *Rhinopithecus roxellana* were searched in the *N. parkeri* genome with BLAST+ (69), and then gene structure was identified using GeneWise (70). For RNA sequences-based methods, the full-length transcriptome sequences from PacBio Sequel platform were mapped to the *N. parkeri* genome for gene structure prediction using GMAP (71). Finally, genes predicted from the above methods were integrated by EvidenceModeler (EVM) (72) into a non-redundant consensus of gene sets. Five different public protein databases, including SwissProt, TrEMBL (73), KEGG (74), Gene Ontology (GO) (75), and NR (NCBI non-redundant protein sequence database) (76), were selected for gene functional annotation of *N. parkeri* using Blast+ (69). The integrated methods yielded a nonredundant gene set composed of 22,884 protein-coding genes (accounting for 99.58% of total genes) in the *N. parkeri* genome (**Supplementary Table 6**), with an average exon number per gene of 7.78. The average transcript length, average coding sequence (CDS) length, average exon length and average intron length were 31,131 bp, 1,382 bp, 177 bp, and 4,381 bp, respectively (**Supplementary Table 7**).

We annotated the repetitive sequences in the *N. parkeri* genome using both the homology prediction method and the *de novo* prediction method, accounting for 58.90% of the genome. First, RepeatMasker and RepeatProteinMask (77) were used based on RepBase TE library (<https://www.girinst.org/repbase/>). As a result, most of the repeated sequences were transposable elements (TEs), occupying 55.20% (1.36 Gb) of the assembly (**Supplementary Table 8**). Then, non-coding RNAs (including microRNAs) were identified through aligning the *N. parkeri* genome to the Rfam database (78) with default parameters. The alignments with an E-value < 10<sup>-6</sup> were considered statistically significant and their corresponding genomic regions were annotated as conserved non-coding RNA genes. Infernal (79) was used to filter raw results to obtain the final non-coding RNAs. These non-coding RNAs were further categorized into microRNA (miRNA), transfer RNA (tRNA), ribosomal RNA (rRNA), small nuclear RNA (snRNA) (**Supplementary Table 9**). The raw sequences for the whole genome assembly and annotation information have been deposited in the Genome Sequence Archive (GSA) of National Genomics Data Center (NGDC) at <https://ngdc.cncb.ac.cn/gsa/> (accession: CRA004362). The whole-genome assembly data have been deposited in the Genome Warehouse (GWH) of NGDC at <https://bigd.big.ac.cn/gwh> under accession number GWHBCKU00000000. The annotation files can be found in Figshare at [https://figshare.com/projects/Genomic\\_data\\_of\\_Nanorana\\_parkeri/116061](https://figshare.com/projects/Genomic_data_of_Nanorana_parkeri/116061).

#### Library construction and transcriptome sequencing of skin samples

To interpret how defense-related genes change in expression with ongoing UV exposure, we collected dorsal skin tissue of three to four individuals at each time point (in the time-course of UV exposure) in each species for mRNA-seq. Total RNA was extracted using TRIzol reagent (Takara) and RNeasy Mini Kit (Qiagen, Valencia, CA). RNA purity was assessed using kaiaoK5500@Spectrophotometer (Kaiao, Beijing, China), the integrity and concentration was assessed using RNA Nano 6000 Assay Kit of the Bioanalyzer 2100 system (Agilent Technologies, CA, USA). A total of 2 µg RNA per sample was used as input material for the RNA sample preparations. Sequencing libraries were generated using NEBNext® Ultra™ RNA Library Prep Kit for Illumina® (#E7530L, NEB, USA) following the manufacturer's recommendations. Briefly, mRNA was purified from total RNA using poly-T oligo-attached magnetic beads. Fragmentation was carried out using divalent cations under elevated temperature in NEBNext First Strand Synthesis Reaction Buffer (5X). First strand cDNA was synthesized using random hexamer primer and RNase H. Second strand cDNA synthesis was subsequently performed using buffer, dNTPs, DNA polymerase I and RNase H. The library fragments were purified with QiaQuick PCR kits and elution with EB buffer, then terminal repair, A-tailing and adapter added were implemented. RNA concentration of library was measured using Qubit® RNA Assay Kit in Qubit® 3.0 to preliminary quantify and then dilute to 1 ng/µl. Insert size was assessed using the Agilent Bioanalyzer 2100 system (Agilent Technologies, CA, USA), and qualified insert size was accurate quantification using StepOnePlus™ Real-Time PCR System (Library valid concentration >10 nM). The clustering of the index-coded samples was performed on a cBot cluster generation system using HiSeq PE Cluster Kit v4-cBot-HS (Illumina) according to the manufacturer's instructions. After cluster generation, the libraries were sequenced on an Illumina platform and 150 bp paired-end reads were generated. Sequencing reads that contained low-quality, adaptor-polluted, or high content of unknown base reads were removed.

### ***de novo* transcript assemblies of *N. phrynooides* and *Q. spinosa***

For *N. phrynooides* and *Q. spinosa*, for which reference genomes were lacking, clean reads from unexposed group were merged for *de novo* assembly using Trinity (80) with default settings (`-min_contig_length 150 -min_kmer_cov 3 -min_glue 3 -bfly_opts 'V 5 -edge_thr=0.1 -stderr`). And then the reference transcript was produced by eliminating redundant contigs upon assembly with CD-HIT (81). To produce longer and more complete consensus sequences, the TGICL pipeline was used to cluster and assemble sequences with CAP3 (82). TransRate (83) was used to evaluate the quality of the reference transcript based on common statistical indexes, including number of contigs, mean contig length, N50 values, and GC% (Supplementary Table 10). The clean reads of mRNA-seq of studied species in this paper are given in the GSA of NGDC under the accession number CRA004830.

### **Orthologs determination**

A modified reciprocal best hit method (version 0.6.9 "crb-blast") (84) was used to identify orthologous genes between the transcript assemblies (*N. phrynooides* and *Q. spinosa*) and the chromosome-level genome of *N. parkeri* with high accuracy. All of the orthologs were aligned with FasParser (85). The coding region of each assembled contig was determined using TransDecoder (version 3.0.1 with "-m 50" option) (86). If more than one open reading frame (ORF) was predicted, the one with maximum similarity to the sequence in *N. parkeri* was chosen. Prank (87) and Gblocks (88) were used to align each gene into a consensus 1:1 orthologous gene set (Supplementary Data3) for subsequent evolutionary analyses. To reduce false positives, alignments with a final length of less than 120 bp were discarded. Because a high mean identity ratio (MIR) is assumed to indicate a accurate orthology prediction, we estimated the MIR for each alignment to evaluate the quality of our orthologous gene set.

### **Expression abundance calculation**

For *N. parkeri* with a chromosome-level genome, all of the clean reads obtained from mRNA-seq were mapped to the reference genome using HISAT2 (89) (`-phred33 -sensitive -no-discordant -no-mixed -l 1 -X 1000`). SAMtools (90) was used to sort and convert the SAM files to BAM files. Then, StringTie (91) (`-f 0.3 -j 3 -c 5 -g 100 -s 10000 -p 8`) was used to calculate transcript expression levels. A Python script (prepDE.py) was used to extract read count information from the files generated by StringTie. For *N. phrynooides* and *Q. spinosa*, clean reads were mapped to the corresponding reference transcript using Bowtie2 (92) (`-q -phred64 -sensitive -dpad 0 -gbar 99999999 -mp 1,1 -np 1 -score-min L,0,0.1 -l 1 -X 1000 -no-mixed -no-discordant -p l -k 200`). We calculated the expression (FPKM) of each transcript with RSEM (93) for each individual. A heatmap of gene expression was drawn using the eGPS (94) based on Z-scores-normalized FPKM values.

### **Temporal clustering of genes from time-course expression profiles**

We obtained a gene expression profile along with a UV-exposure timeline for each species. To trace the changing pattern of gene expression, we used Short Time-series Expression Miner (STEM) software (version 1.3.12) (37) to classify significant temporal groups. Before implementing STEM, we calculated the median gene expression value at that time point and normalized the median value with the  $\log_2$  function. The normalized expression dataset was used as the input for STEM. The default parameters with "Log normalize data" as the data info and "STEM Clustering Method" as the clustering method, were selected. The cluster results from STEM (Supplementary Fig. 6) indicated four major temporally clustered groups of genes in *N. parkeri* based on changes in their expression patterns: genes with gradual decreases in expression (Clustering Profile #10), genes with gradual increases in expression (Clustering Profile #39), genes with early-phase (at around 0.5 h of time-course) upregulation (Clustering Profiles #44 and #43) and genes with later-phase (at around 8 h of time-course) upregulation (Clustering Profiles #27 and #28). The genes showing gradual decreases and increases in expression were rendered separately to display the results of functional enrichment analysis with Metascape (95).

### **Identification of co-expressed genes in temporal groups**

To identify the critical genes showing early-phase upregulation and later-phase upregulation, the WGCNA package (32) was used to identify coexpressed genes that were strongly related to specific temporal groups (with options “unsigned correlation” and “minimum cluster size = 30”). The Benjamini-Hochberg method was used to correct for multiple testing when calculating the correlation between modules and time points (Supplementary Fig. 7). The genes that were highly correlated with a module ( $MM > 0.6$ ,  $P$ -value  $< 0.05$ ) were considered as co-expressed genes in the temporal groups. GO enrichment analyses on genes within each of these temporal groups were performed using Metascape. The gene list and correlation with modules, as well as respective GO terms in each temporal group can be found in Supplementary Tables 3–6.

### miRNA sequencing, annotation and expression calculation

Conserved miRNAs that were predicted *in silico* could be masked as transposable elements (TEs) due to sequence similarity between them. In addition, novel miRNAs in *N. parkeri* could easily be missed. To confirm whether there are novel miRNAs that may have evolved as a UV defense in *N. parkeri*, we performed miRNA-seq analysis of the same individual samples ( $n = 19$  for *N. parkeri*;  $n = 24$  for *N. phrynooides*;  $n = 14$  for *Q. spinosa*) used for mRNA-seq. RNA extraction and quality assessment were performed following the above protocols. Total RNA was separated by 15% agarose gels to extract the small RNA (18-30 nt). After precipitation by ethanol and centrifugal enrichment of the small RNA sample, the library was prepared according to the method and process of Small RNA Sample Preparation Kit (Illumina, RS-200-0048). The primary steps of this procedure are as follows: (1) Connection of the 3' adaptor to the separated small RNA. (2) Connection of the 5' adaptor to the separated small RNA. (3) RT-PCR. (4) Recycling strips of 145-160bp (22-30nt RNA). The RNA concentration of the library was measured using a Qubit® RNA Assay Kit in Qubit® 2.0 to quantify and then dilute to 1ng/μl. Insert size was assessed using the Agilent Bioanalyzer 2100 system (Agilent Technologies, CA, USA), and after the insert size was found to be consistent with expectations, insert size was accurately quantified using Taqman fluorescence probe of AB Step One Plus Real-Time PCR system (Library valid concentration  $> 2$ nM). The qualified libraries were sequenced using an Illumina platform to generate 50 bp single-end reads. Sequencing reads that contained low-quality, adaptor-polluted, or high content of unknown base reads were filtrated. The 3' adapters were clipped from the sequencing reads. Reads with the same sequence and those with a length shorter than 15 bp after clipping the 3' adapter were discarded. The clean reads of miRNA sequencing of studied species in this paper are given in the GSA of NGDC under the accession number CRA005235.

The filtered reads were mapped to the corresponding genome (*N. parkeri*) or reference transcripts (*N. phrynooides* and *Q. spinosa*) using Bowtie (-best -strata -v 0 -k 100) (96) and then analyzed with miRDeep2 (97) to annotate mature miRNAs and precursors. The annotation was based on known miRNAs (from the available well annotated genomes including *Xenopus laevis*, *X. tropicalis*, *Anolis carolinensis*, *Gallus gallus*, *Homo sapiens*) curated in miRBase (release 22) (98) without any mismatches allowed. miRNAs with a read counts  $< 5$  and a true positive probability  $< 60\%$  were excluded from downstream analyses. This analysis resulted in two categories of known and novel miRNAs. To exclude sequencing noise falsely classified as known or novel miRNAs, we also predicted the reliable miRNAs for each individual using the miRNA-seq data. In this screen, if miRNA expression was detected in at least two of the three (or four) individuals in one time point of UV exposure, we considered them as reliable miRNAs. The numbers of known and novel miRNAs identified in each species are listed in Supplementary Data 8.

The miRNAs of each species were mapped to the respective genome or transcripts for abundance quantification. Some miRNA reads were counted multiple times when miRDeep2 assigned them to mature miRNAs, and some were mapped to multiple genomic loci. Therefore, the normalization of miRNA reads was performed by dividing the reads quantified by miRDeep2 with the total miRNA reads quantified by Bowtie. We used the normalized data as our miRNA expression data, and  $\log_2$ -transformed data (Supplementary Data 9) were used for further analyses.

### miRNA target prediction

mRNA and miRNA expression data from the same individual were combined as the input data for WGCNA to identify co-expressed miRNAs and mRNAs in the early-phase temporal group and later-phase temporal group. miRNAs showed a significant negative correlation ( $MM < 0$ ,  $P$ -value  $< 0.05$ ) with a temporal group were selected as co-expressed miRNA candidates (Supplementary 10). To identify co-expressed miRNAs in gradually increasing group and gradually decreasing group, expression profiles of the total miRNAs were further clustered using STEM (Supplementary Fig. 11). In the *N. parkeri* STEM results, the miRNAs in Clustering Profile #10 and Clustering Profile #39 were separately considered candidates for the gradually increasing and gradually decreasing temporal groups. The mRNA targets of all the co-expressed miRNAs were predicted with TargetScan (version 7.1) (99) with the parameter “Total context++ score  $< -0.1$ ”. A miRNA may have many potential target genes. To identify which miRNAs explicitly function in regulating the expression of genes involved in the UV defense systems of *N. parkeri*, we further compared changes in the expression patterns of a miRNA and its predicted mRNA targets. Only those miRNAs that showed a significant negative correlation (showing expression inhibition as a function) with their predicted targets in a specific temporal group were retained. These miRNAs were considered modulators of gene expression in UV defense systems. The correlation of miRNAs and target mRNA in expression was qualified by Spearman's rank correlation coefficient test in R (Supplementary Table 11).

### Evolutionary analyses

Based on the phylogenetic relationships of the studied species (46), codeml was used to estimate  $dN$ ,  $dS$ , and  $dN/dS$  values with the free ratio model (“model=1”). An improved branch-site model (Null hypothesis: model = 2, NSsites = 2, fix\_omega = 1, omega =1; Alternative hypothesis: model = 2, NSsites = 2, fix\_omega = 0, omega = 1) in PAML (47) was used to identify genes showing positive selection along the *N. parkeri* branch, which was assigned as the foreground branch. A likelihood-ratio test (LRT) was used to compare the observed positive selection to a null model, and the corresponding  $P$ -value was calculated. Positively selected sites were deduced through Bayesian empirical Bayes (BEB) analysis.

## ***In vitro* synthesis of tyrosinase and confirmation of its activity**

To investigate the activity of tyrosinase, we separately synthesized DNA sequences encoding the *N. parkeri* and *Q. spinosa* tyrosinase protein sequence *in vitro* (see **Supplementary Fig. 13** for synthesized protein expression). We inserted the synthesized tyrosinase sequences into PET-32a bacterial plasmids, which were then transferred into BL21 competent cells (TSV-A09, TSINGKE, Kunming, China). The bacterial strains transfected with the recombinant plasmid were inoculated in LB liquid medium resistant to ampicillin (A610028, Sangon Biotech, Shanghai, China), and cultured at 37°C with agitation 180 rpm to OD<sub>600</sub> = 0.6. The recombinant fusion tyrosinases were isolated and purified under 4°C. Then, the tyrosinase was expressed with 200mM CuSO<sub>4</sub> (A600063-0500, Sangon Biotech, Shanghai, China) and 100mM IPTG (I6148, Macklin, Shanghai, China) induction at 28°C with shaking (100rpm) for 10 hours, and purified under 4°C by Ni-NTA agarose column (30230, QIAGEN, Valencia, CA, USA), according to the instruction. With the buffer (15μM CuSO<sub>4</sub> 50mM Na<sub>2</sub>HPO<sub>4</sub>, pH 6.2), the tyrosinase solution was reacted with the substrate L-DOPA (D9628-5G, Sigma-Aldrich, MO, American) at concentrations of 0.625mM, 1.5mM, 2.5mM, 5mM and 10mM. The absorbance at 475nm was measured with Microplate Reader (Epoch, BioTek, VT, American) at 1-minute intervals, and monitored for 1 h. The dynamics of the tyrosinase catalysis are showed in a fitted curve generated with the Line weaver-Burk equation.

## **Statistical analysis**

For experiments with replicates, the results are shown as mean ± s.d. with replicates from independent biological experiments. Two-tailed *t*-tests were executed using 't.test' in R (parameters, alternative = 'two.sided'; paired = TRUE). Spearman's rank correlation coefficient test statistic was performed using the 'cor.test' function in R (parameters, method = 'spearman'; exact = TRUE).

## **Data availability**

Data are available in the Genome Sequence Archive (GSA) (100) in National Genomics Data Center (NGDC) (101), China National Center for Bioinformatics / Beijing Institute of Genomics (CNCB/BIG), Chinese Academy of Sciences (CAS) at <https://ngdc.cncb.ac.cn/gsa/> (GSA accessions: CRA004362, CRA004830 and CRA005235), the Genome Warehouse (GWH) of NGDC at <https://bigd.big.ac.cn/gwh> (accession: GWHBCKU000000000) and Figshare ([https://figshare.com/projects/Genomic\\_data\\_of\\_Nanorana\\_parkeri/116061](https://figshare.com/projects/Genomic_data_of_Nanorana_parkeri/116061)).

## **Declarations**

### **Acknowledgments**

We thank Yong-Bin Chen, Bao-Wei Jiao, Ju-Min Zhou, Zhen Liu, Bo Zhao and Jing Chai for helpful discussions; Bao-Lin Zhang, Yong Shao, Wei Xu for assistance in collections; Hong-Man Chen for technical support in the lab.

### **Funding:**

Strategic Priority Research Program of Chinese Academy of Sciences XDPB17

The Second Tibetan Plateau Scientific Expedition and Research Program 2019QZKK0501

Strategic Priority Research Program of Chinese Academy of Sciences XDA20050201

Large Research Infrastructure Funding of Animal Branch of the Germplasm Bank of Wild Species of Chinese Academy of Sciences (JC)

Natural Science Foundation of China 31671326 (YBS)

Yunnan Fundamental Research Projects NO. 202101AV070009 (YBS)

Natural Science Foundation of China 81760648 (XWY)

Open Project from the State Key Laboratory of Genetic Resources and Evolution GREKF20-02

Chinese Academy of Sciences President's International Fellowship Initiative 2018VBA0039 (DMH)

Chinese Academy of Sciences President's International Fellowship Initiative 2017VBA0003 (RWM)

National Sciences and Engineering Research Council of Canada Discovery Grant A3148 (RWM)

State Scholarship Fund NO. 201904910862 (TTF)

### **Author contributions:**

Research design: J.C., Y.-P.Z., D.M.H., R.L., Y.Z., Y.B.S.

Investigation: T.T.F., Y.B.S., W.G., C.B.L., C.H.Y., X.W.Y., Y.Z., X.Q.L., S.H.

## Competing interests

Authors declare that they have no competing interests.

## Extended data

Extended Data 1 Photographs and statistics of histological skin sections in studied species.

Extended Data 2 Metabolomics identification.

Extended Data 3 Orthologous genes across studied species.

Extended Data 4 Genes of early-phase up-regulation and associated functional enrichments.

Extended Data 5 Genes of later-phase up-regulation and associated functional enrichments.

Extended Data 6 Genes that gradually increased in expression and associated functional enrichments.

Extended Data 7 Genes that gradually decreased in expression and associated functional enrichments.

Extended Data 8 Conservative and novel miRNAs predicted in studied frogs.

Extended Data 9 Normalized expression levels of miRNAs in studied frogs.

Extended Data 10 List of PSGs and associated functional enrichments.

## References

1. Sivasakthivel T., Siva Kumar Reddy K. K. Ozone layer depletion and its effects: a review. *Inter. Jour. of Env. Sci. and Dev.* **2**, 30–37 (2011).
2. Anderson G. J., Margitan J. J., Stedman H. D. Atomic chlorine and the chlorine monoxide radical in the stratosphere: three in situ observations. *Science* **198**, 501–503 (1977).
3. Cadet J., Douki T., Ravanat L. J. Oxidatively generated damage to cellular DNA by UVB and UVA radiation. *Photochem. Photobiol.* **91**, 140–55 (2015).
4. Lo A. J., Fisher E. D. The melanoma revolution: From UV carcinogenesis to new era in therapeutics. *Science* **346**, 945–949 (2014).
5. Dyck J. Structure and colour-production of the blue barbs of *Agapornis roseicollis* and *Cotinga maynana*. *Z. Zellforsch. Mikrosk. Anat.* **115**, 17–29 (1971).
6. Jablonski G. N., Chaplin G. Human skin pigmentation as an adaptation to UV radiation. *Proc. Natl. Acad. Sci. U.S.A.* **107**, 8962–8968 (2010).
7. Lin Y. J., Fisher E. D. Melanocyte biology and skin pigmentation. *Nature* **445**, 843–850 (2007).
8. Matheu A. et al. Delayed ageing through damage protection by the Arf/p53 pathway. *Nature* **448**, 375–379 (2007).
9. Porter W. P., Norris K. S. Lizard reflectivity change and its effect on light transmission through body wall. *Science* **163**, 482–484 (1969).
10. Yang H. et al. Antioxidant peptidomics reveals novel skin antioxidant system. *Mol. Cell Proteomics* **8**, 571–583 (2009).
11. Yang X. W. et al. Rich diversity and potency of skin antioxidant peptides revealed a novel molecular basis for high-altitude adaptation of amphibians. *Sci. Rep.* **6**, 19866 (2016).
12. Yu L., Wang G. D., Ruan J. et al. Genomic analysis of snub-nosed monkeys (*Rhinopithecus*) identifies genes and processes related to high-altitude adaptation. *Nat. Genet.* **48**, 947–952 (2016).
13. Poljsak B., Dahmane R., Godic A. Skin and antioxidants. *J. Cosmet. Laser Ther.* **15**, 107–113 (2013).
14. Olin-Sandoval V. et al. Lysine harvesting is an antioxidant strategy and triggers underground polyamine metabolism. *Nature* **572**, 249–253 (2019).
15. Nassour J. et al. Defective DNA single-strand break repair is responsible for senescence and neoplastic escape of epithelial cells. *Nat. Commun.* **7**, 10399 (2016).
16. Rastogi P. R., Kumar A. Richa, Tyagi B. M., Sinha P. R. Molecular mechanisms of ultraviolet radiation-induced DNA damage and repair. *DNA Damage, Mutagenesis, and DNA Repair 2010:592080* (2010).
17. Mendez F., Sandigursky M., Franklin A. W., Kenny K. M., Kurekattil R., Bases R. Heat-shock proteins associated with base excision repair enzymes in hela cells. *Radiat. Res.* **153**, 186–195 (2000).
18. Jarosz F. D., Lindquist S. Hsp90 and environmental stress transform the adaptive value of natural genetic variation. *Science* **330**, 1820–1824 (2010).
19. Li J. T. et al. Comparative genomic investigation of high-elevation adaptation in ectothermic snakes. *Proc. Natl. Acad. Sci. U.S.A.* **115**, 8406–8411 (2018).

20. Blaustein R. A., Kiesecker M. J. Complexity in conservation: lessons from the global decline of amphibian populations. *Ecol. Lett.* **5**, 597–608 (2002).
21. Granstein D. R., Parrish A. J., Mcauliffe J. D., Waltenbaugh C., Greene I. M. Immunologic inhibition of ultraviolet radiation-induced tumor suppressor cell activity. *Science* **224**, 615–617 (1984).
22. Alton A. L., Franklin E. C. Drivers of amphibian declines: effects of ultraviolet radiation and interactions with other environmental factors. *Clim. Chang. Responses* **4**:6 (2017).
23. Che J. et al. Spiny frogs (Paini) illuminate the history of the Himalayan region and southeast Asia. *Proc. Natl. Acad. Sci. U.S.A.* **107**, 13765–13770 (2010).
24. Yang C. H., Fu T. T. et al. Comparative skin histology of frogs reveals high-elevation adaptation of the Tibetan *Nanorana parkeri*. *Asian Herpetological Research* **10**, 79–85 (2019).
25. Verdin E. NAD<sup>+</sup> in aging, metabolism, and neurodegeneration. *Science* **350**, 1208–1213 (2015).
26. Stuyvesant V., Jolley W. Anti-inflammatory activity of d- $\alpha$ -Tocopherol (Vitamin E) and linoleic acid. *Nature* **216**, 585–586 (1967).
27. Marieb N. E. *Human anatomy & physiology* (Benjamin Cummings, San Francisco, 2001).
28. Morgan V. R. *Handbook of Small Animal Practice* (Fifth Edition) (Elsevier, 2008).
29. McIntire L. S. et al. Identification and characterization of the vesicular GABA transporter. *Nature* **389**, 870–876 (1997).
30. Sun Y. B. et al. Whole-genome sequence of the Tibetan frog *Nanorana parkeri* and the comparative evolution of tetrapod genomes. *Proc. Natl. Acad. Sci. U.S.A.* **112**, 1257–1262 (2015).
31. Ernst J., Bar-Joseph Z. STEM: a tool for the analysis of short time series gene expression data. *BMC Bioinformatics* **7**, 191–201 (2006).
32. Langfelder P., Horvath S. WGCNA: an R package for weighted correlation network analysis. *BMC Bioinformatics* **9**, 559–572 (2008).
33. Joyal S. J., Nim S., Zhu T. et al. Subcellular localization of coagulation factor II receptor-like 1 in neurons governs angiogenesis. *Nat. Med.* **20**, 1165–1173 (2014).
34. Teng M. W. L., Bowman P. E., McElwee J. J., Smyth J. M., Casanova J. L., Cooper M. A., Cua D. J. IL-12 and IL-23 cytokines: from discovery to targeted therapies for immune-mediated inflammatory diseases. *Nat. Med.* **21**, 719–729 (2015).
35. Wolf A. J., Underhill D. M. Peptidoglycan recognition by the innate immune system. *Nat. Rev. Immunol.* **18**, 243–254 (2018).
36. Morad S., Cabot M. Ceramide-orchestrated signaling in cancer cells. *Nat. Rev. Cancer* **13**, 51–65 (2013).
37. Welch H. et al. P-Rex1, a PtdIns(3,4,5)P<sub>3</sub>- and G- $\alpha$ -beta-regulated guanine-nucleotide exchange factor for Rac. *Cell* **108**, 809–821 (2002).
38. Grundemann D., Gorboulev V., Gambaryan S., Veyhl M., Koepsell H. Drug excretion mediated by a new prototype of polyspecific transporter. *Nature* **372**, 549–552 (1994).
39. Worby C. A., Dixon J. E. Sorting out the cellular functions of sorting nexins. *Nat. Rev. Mol. Cell Biol.* **3**, 919–931 (2002).
40. Ressler K. J. et al. Post-traumatic stress disorder is associated with PACAP and the PAC1 receptor. *Nature* **470**, 492–497 (2011).
41. Buscail L. et al. Inhibition of cell proliferation by the somatostatin analogue RC-160 is mediated by somatostatin receptor subtypes SSTR2 and SSTR5 through different mechanisms. *Proc. Natl. Acad. Sci. U.S.A.* **92**, 1580–1584 (1995).
42. Wieskopf J. S., Mathur J., Limapichat W. et al. The nicotinic  $\alpha 6$  subunit gene determines variability in chronic pain sensitivity via cross-inhibition of P2X2/3 receptors. *Sci. Transl. Med.* **7**, 287ra72 (2015).
43. Jia Q., Sieburth D. Mitochondrial hydrogen peroxide positively regulates neuropeptide secretion during diet-induced activation of the oxidative stress response. *Na. Commun.* **12**, 2304 (2021).
44. Gentile M., Latonen L., Laiho M. Cell cycle arrest and apoptosis provoked by UV radiation–induced DNA damage are transcriptionally highly divergent responses. *Nucleic Acids Res.* **31**, 4779–4790 (2003).
45. Fraser H. B. Gene expression drives local adaptation in humans. *Genome Res.* **23**, 1089–1096 (2013).
46. Sun Y. B., Fu T. T. et al. Species groups distributed across elevational gradients reveal convergent and continuous genetic adaptation to high elevations. *Proc. Natl. Acad. Sci. U.S.A.* **115**, E10634–10641 (2018).
47. Yang Z. H. PAML 4: Phylogenetic analysis by maximum likelihood. *Mol. Biol. Evol.* **24**, 1586–1591 (2007).
48. Körner A., Pawelek J. Mammalian tyrosinase catalyzes three reactions in the biosynthesis of melanin. *Science* **217**, 1163–1165 (1982).
49. Jeannie Allen. Ultraviolet radiation: How it affects life on earth. (Earth Observatory, September 6, 2001).
50. Gilchrest B. A., Eller M. S. DNA photodamage stimulates melanogenesis and other photoprotective responses. *J. Investig. Dermatol. Symp. Proc.* **4**, 35–40 (1999).
51. Scott M. C. et al. Human melanocortin 1 receptor variants, receptor function and melanocyte response to UV radiation. *J. Cell Sci.* **115**, 2349–55 (2002).
52. Cui R. et al. Central role of p53 in the suntan response and pathologic hyperpigmentation. *Cell* **128**, 853–64 (2007).
53. Dunaway S., Odin R., Zhou L. L., Ji L. Y., Zhang Y. H., Kadekaro A. L. Natural antioxidants: multiple mechanisms to protect skin from solar radiation. *Front Pharmacol.* **9** (2018).

54. Galanakis C. M., Tsatalas P., Galanakis I. M. Phenols from olive mill wastewater and other natural antioxidants as UV filters in sunscreens. *Environ. Technol. Innov.* **9**, 160–8 (2018).
55. Muthusamy V., Piva T. J. The UV response of the skin: A review of the MAPK, NFκB and TNFα signal transduction pathways. *Arch. Dermatol. Res.* **302**, 5–17 (2009).
56. Robu M., Shah R. G., Petitsclerc N., Brind'Amour J., Kandan-Kulangara F., Shah G. M. Role of poly(ADP-ribose) polymerase-1 in the removal of UV-induced DNA lesions by nucleotide excision repair. *Proc. Natl. Acad. Sci. USA.* **110**, 1658–1663 (2013).
57. Schwertman P. et al. UV-sensitive syndrome protein UVSSA recruits USP7 to regulate transcription-coupled repair. *Nature Genetics* **44**, 598–602 (2012).
58. Yoo H. et al. CRT3, a sensor and key regulator for melanogenesis, as a tunable therapeutic target for pigmentary disorders. *Theranostics* **11**, 9918–9936 (2021).
59. Greenberg N. M. et al. Rosen, Prostate cancer in a transgenic mouse. *Proc. Natl. Acad. Sci. U.S.A.* **92**, 3439–3443 (1995).
60. Akerström B., Maghzal G. J., Winterbourn C. C., Kettle A. J. The lipocalin alpha1-microglobulin has radical scavenging activity. *J. Biol. Chem.* **282**, 31493–31503 (2007).
61. Want E. J. et al. Global metabolic profiling of animal and human tissues via UPLC-MS. *Nat. Protoc.* **8**, 17–32 (2013).
62. Chin C. S. et al. Phased diploid genome assembly with single-molecule real-time sequencing. *Nat. Methods.* **13**, 1050–1054 (2016).
63. Chen Y. et al. SOAPnuke: a MapReduce acceleration-supported software for integrated quality control and preprocessing of high-throughput sequencing data. *GigaScience* **7**, gix120 (2018).
64. Servant N. et al. HiC-Pro: an optimized and flexible pipeline for Hi-C data processing. *Genome Biol.* **16**, 259–270 (2015).
65. Walker B. J. et al. Pilon: An integrated tool for comprehensive microbial variant detection and genome assembly improvement. *PLoS One* **9**, e112963 (2014).
66. Simão F. A., Waterhouse R. M., Ioannidis P., Kriventseva E. V., Zdobnov E. M. BUSCO: assessing genome assembly and annotation completeness with single-copy orthologs. *Bioinformatics* **31**, 3210–3212 (2015).
67. Burton J. N., Adey A., Patwardhan R. P., Qiu R., Kitzman J. O., Shendure J. Chromosome-scale scaffolding of de novo genome assemblies based on chromatin interactions. *Nat. Biotechnol.* **31**, 1119–1125 (2013).
68. Stanke M., Schöffmann O., Morgenstern B., Waack S. Gene prediction in eukaryotes with a generalized hidden Markov model that uses hints from external sources. *BMC Bioinformatics* **7**, 62–73 (2006).
69. McGinnis S., Madden T. L. BLAST: at the core of a powerful and diverse set of sequence analysis tools. *Nucleic Acids Res.* **32** W20–W25 (2004).
70. Birney E., Clamp M., Durbin R. GeneWise and Genomewise, *Genome Res.* **14**, 988–995 (2004).
71. Wu T. D., Watanabe C. K. GMAP: a genomic mapping and alignment program for mRNA and EST sequences. *Bioinformatics* **21**, 1859–1875 (2005).
72. Haas B. J. et al. Automated eukaryotic gene structure annotation using EVIDENCEModeler and the Program to Assemble Spliced Alignments. *Genome Biol.* **9**, R7.1–R7.22 (2008).
73. Bairoch A., Apweiler R. The SWISS-PROT protein sequence database and its supplement TrEMBL in 2000. *Nucleic Acids Res.* **28**, 45–48, (2000).
74. Ogata H., Goto S., Sato K., Fujibuchi W., Bono H., Kanehisa M. KEGG: Kyoto encyclopedia of genes and genomes. *Nucleic Acids Res.* **27**, 29–34 (1999).
75. Ashburner M. et al. Gene Ontology: tool for the unification of biology. *Nat. Genet.* **25**, 25–29 (2000).
76. Pruitt K. D., Tatusova T., Maglott D. R. NCBI reference sequences (RefSeq): a curated non-redundant sequence database of genomes, transcripts and proteins. *Nucleic Acids Res.* **35**, D501–D504 (2007).
77. Tarailo-Graovac M., Chen N. Using RepeatMasker to identify repetitive elements in genomic sequences. *Curr. Protoc. Bioinformatics Chap. 4*, Unit 4.10 (2009).
78. Kalvari I. et al. Rfam 13.0: shifting to a genome-centric resource for non-coding RNA families. *Nucleic Acids Res.* **46**, D335–D342 (2018).
79. Nawrocki E. P., Eddy S. R. Computational identification of functional RNA homologs in metagenomic data. *RNA Biol.* **10**, 1170–1179 (2013).
80. Grabherr M. G. et al. Full-length transcriptome assembly from RNA-Seq data without a reference genome. *Nat. Biotechnol.* **29**, 644–652 (2011).
81. Fu L., Niu B., Zhu Z., Wu S., Li W. CD-HIT: Accelerated for clustering the next-generation sequencing data. *Bioinformatics* **28**, 3150–3152 (2012).
82. Huang X., Madan A. CAP3: A DNA sequence assembly program. *Genome Res.* **9**, 868–877 (1999).
83. Smith-Unna R., Boursnell C., Patro R., Hibberd J. M., Kelly S. TransRate: reference-free quality assessment of *de novo* transcriptome assemblies. *Genome Res.* **26**, 1134–1144 (2016).
84. Aubry S., Kelly S., Kumpers B. M., Smith-Unna R. D., Hibberd J. M. Deep evolutionary comparison of gene expression identifies parallel recruitment of trans-factors in two independent origins of C4 photosynthesis. *PLoS Genet.* **10**, e1004365 (2014).
85. Sun Y. B. FasParser: A package for manipulating sequence data. *Zool. Res.* **38**, 110–112 (2017).
86. Oakley T. H. et al. Osiris: Accessible and reproducible phylogenetic and phylogenomic analyses within the Galaxy workflow management system. *BMC Bioinformatics* **15**, 230–239 (2014).

87. Löytynoja A. Phylogeny-aware alignment with PRANK. *Methods Mol. Biol.* **1079**, 155–170 (2014).
88. Talavera G., Castresana J. Improvement of phylogenies after removing divergent and ambiguously aligned blocks from protein sequence alignments. *Systematic Biology* **56**, 564–577.
89. Kim D., Langmead B., Salzberg S. HISAT: a fast spliced aligner with low memory requirements. *Nat. Methods* **12**, 357–360 (2015).
90. Li H. A statistical framework for SNP calling, mutation discovery, association mapping and population genetical parameter estimation from sequencing data. *Bioinformatics* **27**, 2987–93 (2011).
91. Perteza M., Perteza G. M., Antonescu C. M., Chang T. C., Mendell J. T., Salzberg S. L. StringTie enables improved reconstruction of a transcriptome from RNA-seq reads. *Nat. Biotechnol.* **33**, 290–295 (2015).
92. Langmead B., Salzberg S. Fast gapped-read alignment with Bowtie 2. *Nat. Methods* **9**, 357–359 (2012).
93. Li B., Dewey C. N. RSEM: accurate transcript quantification from RNA-Seq data with or without a reference genome. *BMC Bioinformatics* **12**, 323–339 (2011).
94. Yu D. et al. eGPS 1.0: comprehensive software for multi-omic and evolutionary analyses. *National Sci. Rev.* **6**, 867–869 (2019).
95. Zhou Y. et al. Metascape provides a biologist-oriented resource for the analysis of systems-level datasets. *Nat. Commun.* **10**, 1523–1533 (2019).
96. Langmead B., Trapnell C., Pop M., Salzberg S. L. Ultrafast and memory-efficient alignment of short DNA sequences to the human genome. *Genome Biol.* **10**, R25.1–R25.10 (2009).
97. Friedlander M. R., Mackowiak S. D., Li N., Chen W., Rajewsky N. miRDeep2 accurately identifies known and hundreds of novel microRNA genes in seven animal clades. *Nucleic Acids Res.* **40**, 37–52 (2012).
98. Kozomara A., Birgaoanu M., Griffiths-Jones S. miRBase: from microRNA sequences to function. *Nucleic Acids Res.* **47**, D155–D162 (2018).
99. Agarwal V., Bell G. W., Nam J-W, Bartel D. P. Predicting effective microRNA target sites in mammalian mRNAs. *eLIFE* **4**, e05005 (2015).
100. Chen T. et al. The Genome Sequence Archive family: toward explosive data growth and diverse data types. *Genomics, Proteomics & Bioinformatics* **2021** (2021).
101. CNGB-NGDC Members and Partners. Database resources of the National Genomics Data Center, China National Center for Bioinformation in 2021. *Nucleic. Acids Res.* **49**, D18–D28 (2020).

## Table

**Table 1. Examples of positively selected genes (PSGs) and enriched functional terms in expression profiles of *N. parkeri*. Bold fonts highlight important PSGs with expression shifts in temporal phases of UV exposure.**

GO	Description	Log(P-value)	Enrichment	PSGs
GO:0002274	Myeloid leukocyte activation	-7.79473	2.88192	<b>CD200<sup>a</sup></b> / <b>CD63<sup>b</sup></b> / <b>AGPAT2<sup>b</sup></b> / <b>FGL2<sup>a</sup></b> / <b>SERPINB1</b> / <b>HEXB</b> / <b>IFNGR1</b> / <b>PSMD1</b> / <b>ADAM9</b> / <b>HEBP2</b> ...
GO:1902166	Negative regulation of intrinsic apoptotic signaling pathway in response to DNA damage by p53 class	-3.70563	13.12877	<b>CD74</b> / <b>CD44</b> / <b>ZNF385A</b> / <b>ATAD5</b>
GO:0046514	Ceramide catabolic process	-2.21143	7.87726	<b>HEXB</b> / <b>ACER3<sup>b</sup></b> / <b>GBA2</b>
R-HSA-1474290	Collagen formation	-2.77837	4.08450	<b>COL6A3<sup>b</sup></b> / <b>LOXL1<sup>a</sup></b> / <b>COL2A1</b> / <b>COL6A1</b> / <b>LAMC2</b> / <b>PLOD1</b> ...
GO:0002694	Regulation of leukocyte activation	-2.329	1.8755	<b>CYLD<sup>a</sup></b> / <b>FLOT2<sup>b</sup></b> / <b>PGLYRP3<sup>b</sup></b> / <b>CD200<sup>a</sup></b> / <b>FGL2<sup>a</sup></b> / <b>CASP3</b> / <b>CD40</b> / <b>CD74</b> / <b>CLPTM1</b> / <b>IGHE</b> / <b>LGALS9</b> / <b>XCL1</b> / <b>SFRP1</b> ...
GO:0010212	Response to ionizing radiation	-3.32193	3.62173	<b>RRM1<sup>d</sup></b> / <b>EGR1<sup>a</sup></b> / <b>MAP3K20<sup>a</sup></b> / <b>CASP3</b> / <b>CRYAB</b> / <b>HSF1</b> / <b>SFRP1</b> / <b>TRIM13</b> / <b>TLK2</b> / <b>COP1</b>
GO:1900034	Regulation of cellular response to heat	-2.40038	3.98848	<b>NUP153<sup>b</sup></b> / <b>BAG1</b> / <b>CREBBP</b> / <b>CRYAB</b> / <b>GSK3B</b> / <b>HSF1</b>
GO:0046148	Pigment biosynthetic process	-2.27779	4.45043	<b>FXN<sup>b</sup></b> / <b>TYR<sup>c</sup></b> / <b>SLC25A38<sup>b</sup></b> / <b>APPL1</b> / <b>SLC24A5</b>
hsa00760	Nicotinate and nicotinamide metabolism	-2.67498	7.24346	<b>AOX1<sup>b</sup></b> / <b>NUDT12<sup>b</sup></b> / <b>NADK</b> / <b>NADK2</b>
hsa00350	Tyrosine metabolism	-2.37062	6.00172	<b>TYR<sup>c</sup></b> / <b>AOX1<sup>b</sup></b> / <b>ADH1A</b> / <b>COMT</b>
GO:0033280	Response to vitamin D	-2.32595	5.83500	<b>TYR<sup>c</sup></b> / <b>KANK2<sup>b</sup></b> / <b>AQP3</b> / <b>SFRP1</b>

early-phase upregulation group; <sup>b</sup>Genes in later-phase upregulation group; <sup>c</sup>Genes in gradually increased group; <sup>d</sup>Genes in gradually decreased group.

# Figures

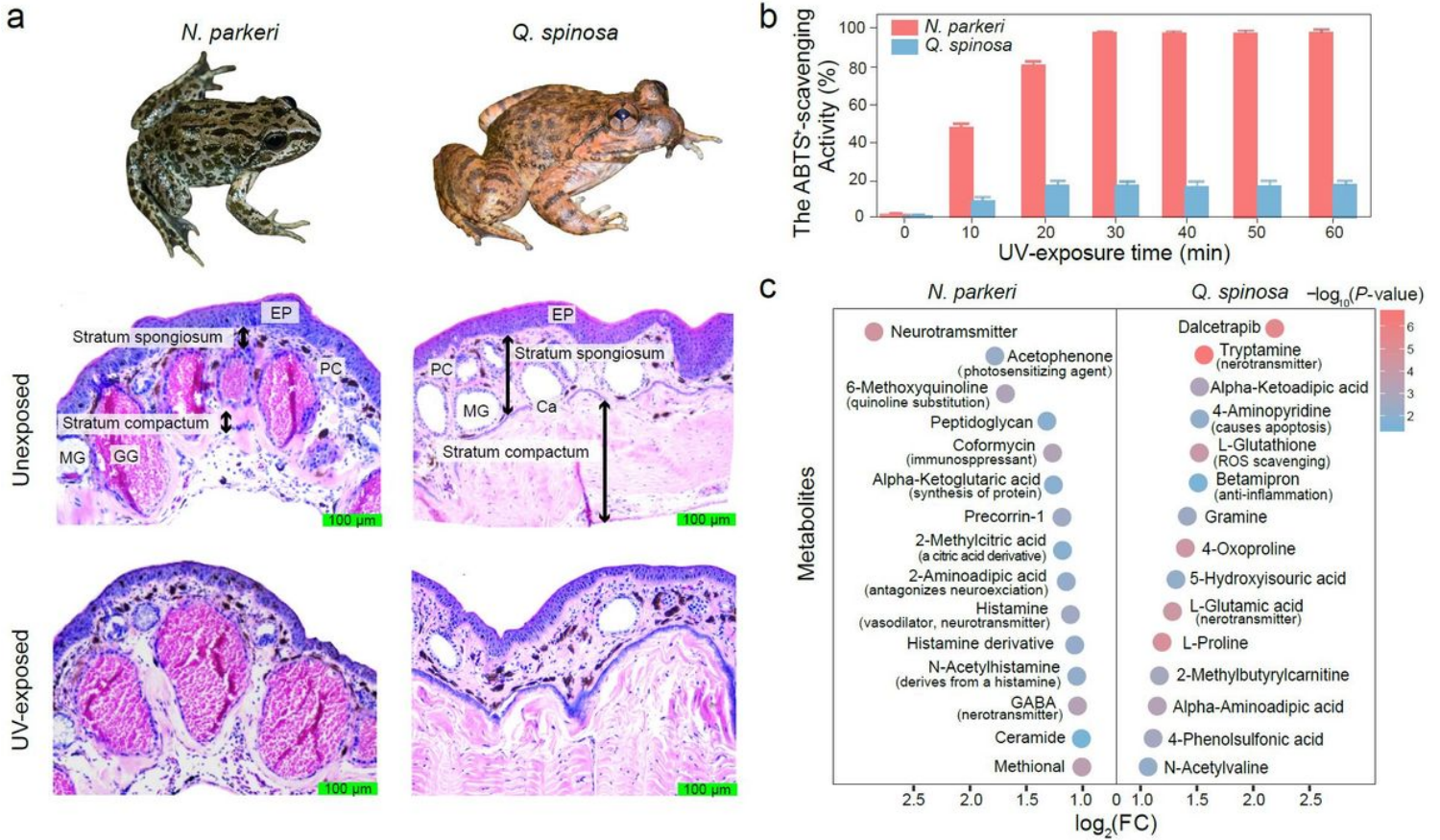


**Figure 1**

**Histological cross-sections and identification of antioxidant capacity and metabolites in frog skin.** **a**, Images separately show the basic skin structures of the unexposed group (upper) and the UV-exposed group (lower; with  $\sim 3.7\text{mW}/\text{cm}^2$  UV exposure for 8 h) in *N. parkeri* and *Q. spinosa* (Ca, calcified layer; EP, epidermis; GG, granular gland; MG, mucous gland; PC, pigment cell). **b**, The ABTS<sup>+</sup>-scavenging tests for each species were performed with a ten-minute interval and the rates of ABTS<sup>+</sup>-scavenging activity (%) were calculated as  $(A_{\text{blank}} - A_{\text{sample}}) \times 100/A_{\text{blank}}$ . Each bar is based on mean  $\pm$  s.e.m. of  $n = 9$  independent experiments. **c**, Examples of metabolites that were significantly up-regulated in the UV-exposed group compared with the unexposed group. Color indicates the significance of the difference with  $P$  values calculated using two-tailed  $t$ -tests and  $\log_2(\text{FC})$  represents the degree of change.

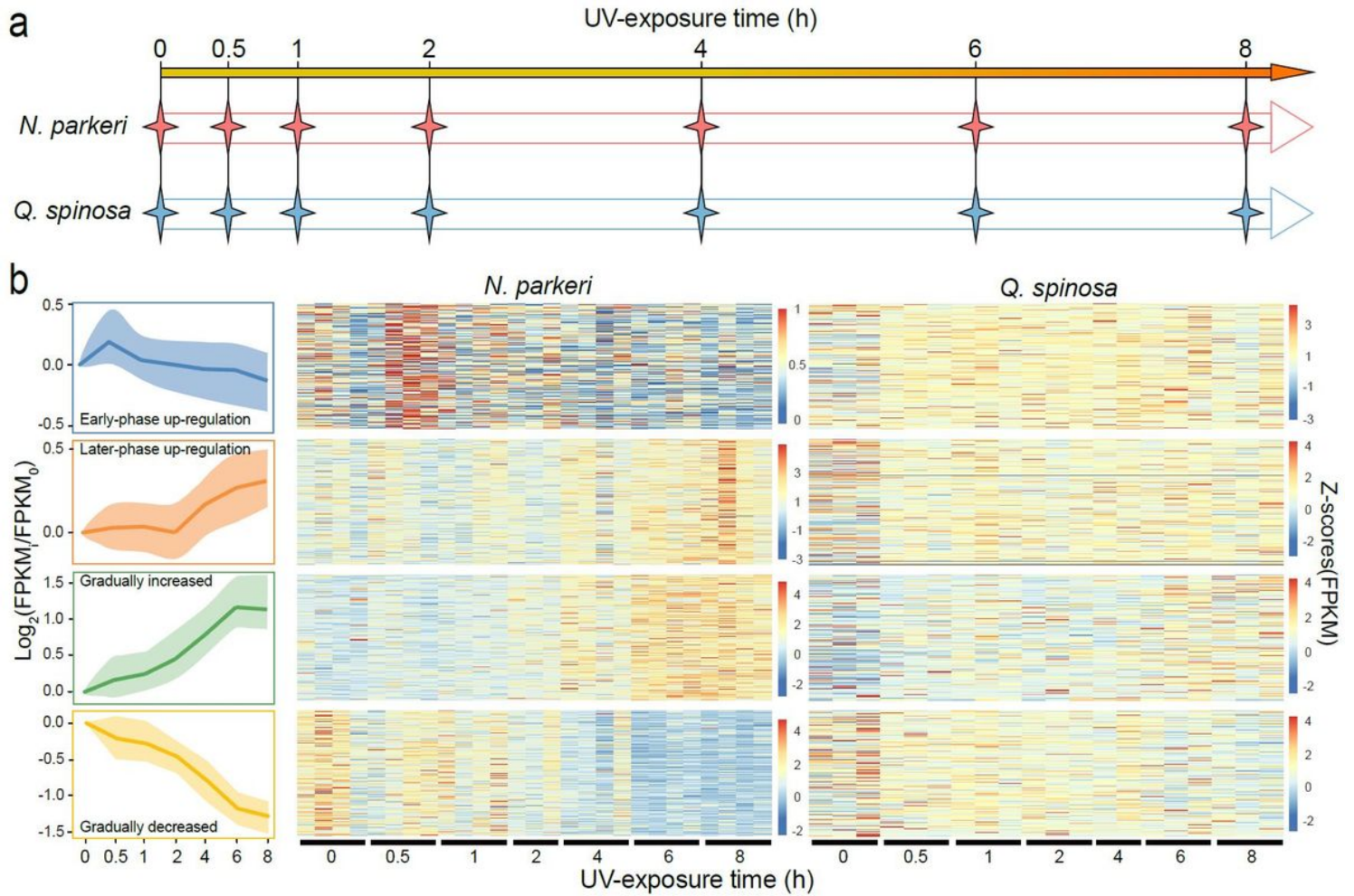
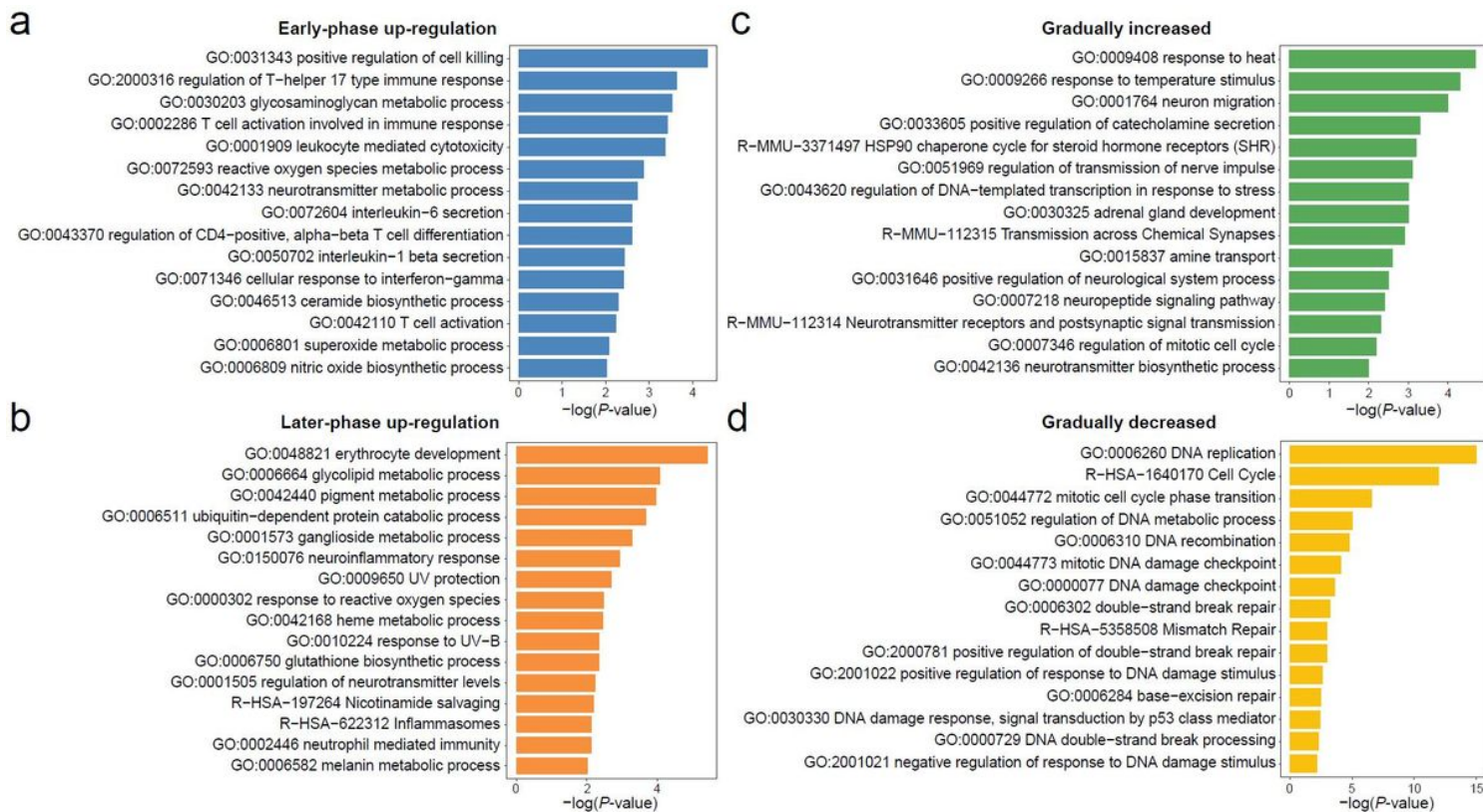


Figure 2

**Experimental proposal and expression heatmaps of genes in four temporal groups throughout UV exposure.** **a**, Schematic shows the experiment procedures of UV exposure in a time course across each species. **b**, Scaled profiles (left panel) were derived from  $\log_2$ -normalized expression changes (FPKM<sub>t<sub>h</sub></sub>/FPKM<sub>0h</sub>) of temporal gene groups in *N. parkeri*, including early-phase up-regulation, later-phase up-regulation, gradually increased expression, and gradually decreased expression. The solid line denotes the median values of expression level and the shaded areas correspond to the range of 25%–75%. The profiles are indicated by a color code used for subsequent analyses. For the expression heatmap of *N. parkeri* (center panel) and *Q. spinosa* (right panel), each row represents an expression level of a gene and color represents an FPKM with Z-scores standardization. FPKM, fragments per kilobase million.



**Figure 3**  
**Functional enrichments of genes in four temporal groups.** **a**, Representative enrichment terms of genes in the early-phase upregulation group. **b**, Representative enrichment terms of genes in the later-phase upregulation group. **c**, Representative enrichment terms of genes in the gradually increased expression group. **d**, Representative enrichment terms of genes in the gradually decreased expression group. Length of a histogram represents  $-\log$ -normalized significance of enrichment with  $P$  value.

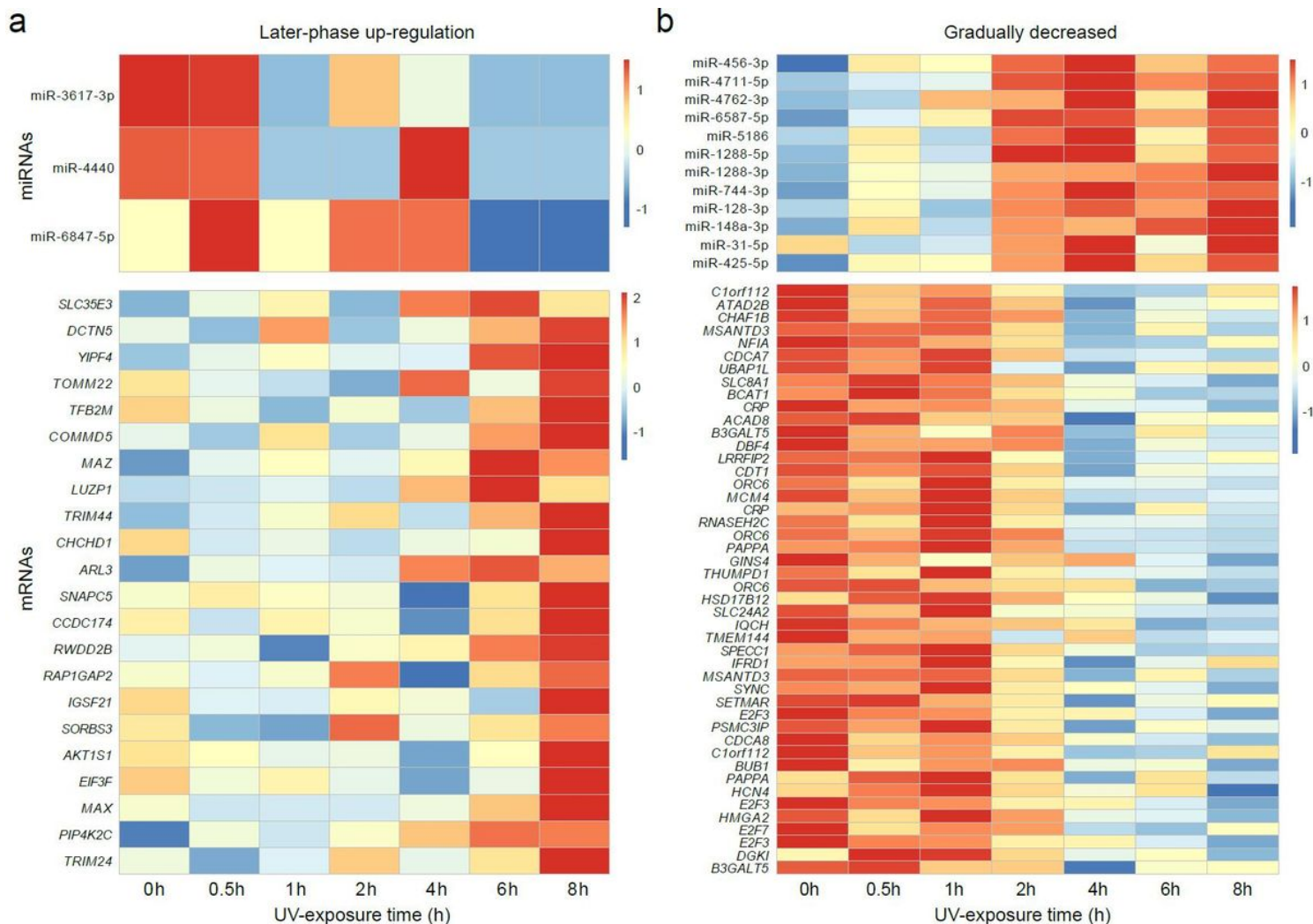


Figure 4

Heatmaps of expression levels of co-expressed miRNA-mRNAs in the later-phase group (a) and the gradually decreased expression group (b) of *N. parkeri*. miRNAs (upper panels) exhibit a significant negative relationship with corresponding mRNA candidates (lower panels) in expression. The Pearson correlation analysis is shown in **Supplementary Table S11**.

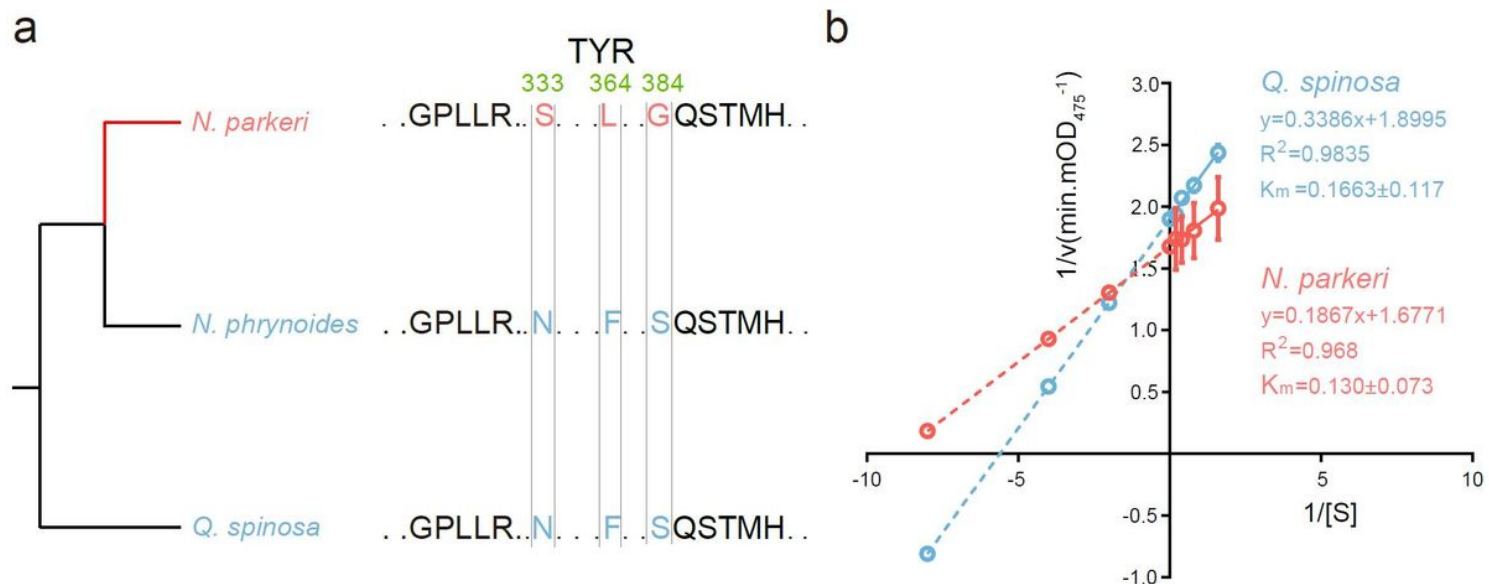


Figure 5

**Amino acids replacements and enzymatic activity identification of tyrosinase (TYR) across *N. parkeri* and *Q. spinosa*.** **a**, Phylogenetic relationships and schematic alignment of TYR amino acid sequences in *N. parkeri* (red) and its lower-elevation relatives (blue). Amino acids replacements unique to *N. parkeri* shown in red font were found to be under positive selection. The reference alignment numbers refer to the amino acid sequence of *N. parkeri*. Single-letter abbreviations for the amino acid residues are as follows: F, Phe; G, Gly; H, His; L, Leu; M, Met; N, Asn; P, Pro; Q, Gln; S, Ser; T, Thr; V, Val. **b**, *In vitro* enzymological kinetic analyses of TYR in *N. parkeri* and *Q. spinosa*.  $K_m$  (Michaelis constant) is used to describe the rate of enzymatic reactions. It is numerically equal to the substrate concentration [S] at which the reaction rate is half of the maximum rate [v] achieved by enzyme. The smaller  $K_m$  represents the stronger affinity the enzyme has for the substrate. Each  $K_m$  value is derived from eight independent experiments which are indicated with circles.  $R^2$  represents the correlation coefficient of the kinetic equation that fits the reaction.

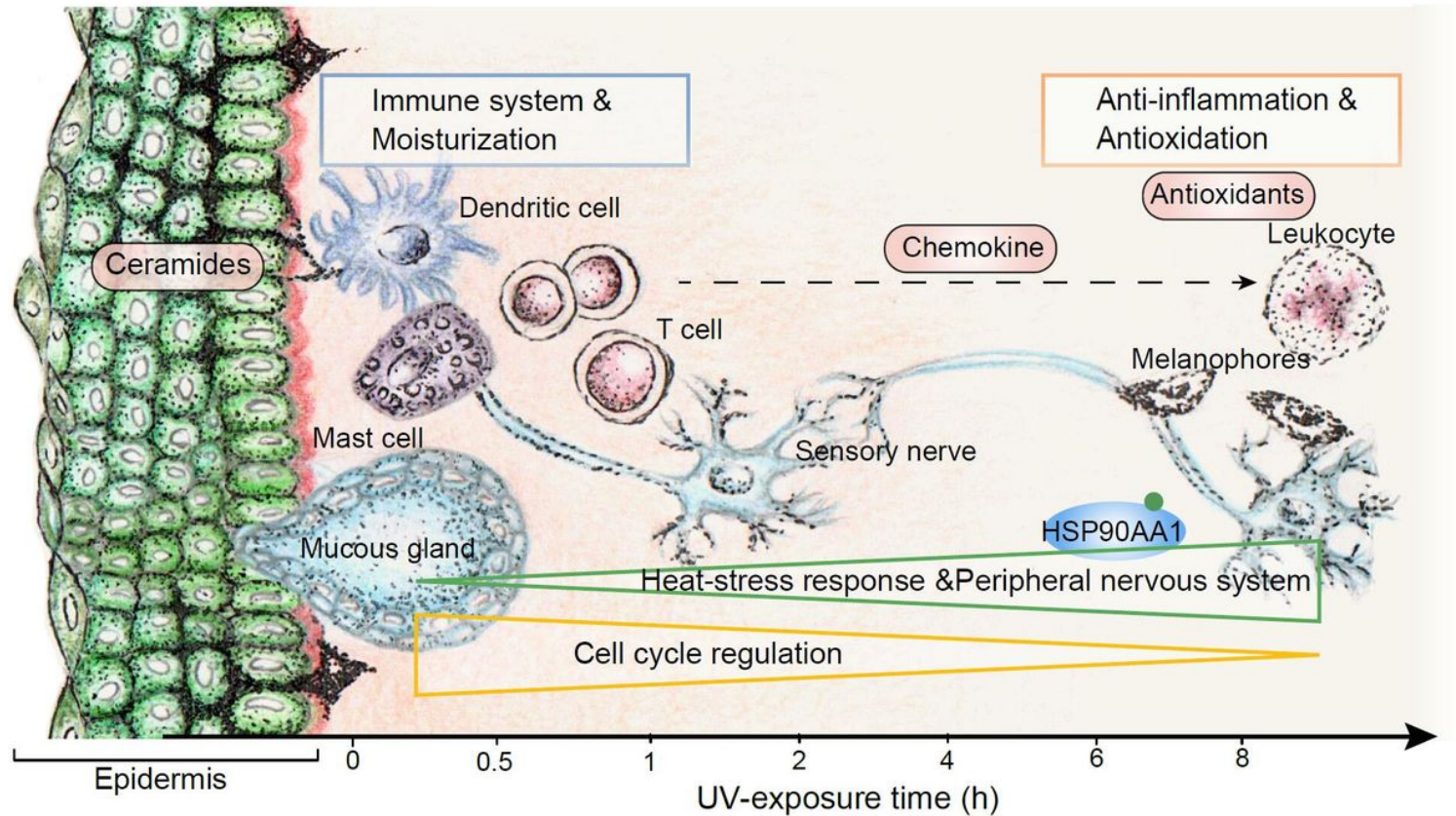


Figure 6

**Molecular dynamics of temporal defense systems against UV exposure in *N. parkeri* skin.** The defense systems and corresponding representative organelles are displayed along the timeline in relationship to their temporal upregulation. Genes in early-phase group are related to immune system and moisturization (blue rectangle) and upregulated at early phase of UV exposure. Immune cells secrete chemokine that induced upregulation of anti-inflammation related genes as well as antioxidative genes (red rectangle) occurred at later-phase of UV exposure. Genes in gradually increased group are related to heat stress response and peripheral nervous system (green triangle) and gradually upregulated in expression. Genes in gradually decreased group function in cell cycle regulation (golden triangle) and gradually downregulated in expression.

## Supplementary Files

This is a list of supplementary files associated with this preprint. Click to download.

- [Supplementaryinformation.docx](#)
- [ExtendedData.zip](#)
- [rs.pdf](#)